Transient Impulses Enhancement Based on Adaptive Multi-scale Improved Differential Filter and Its Application in Rotating Machines Fault Diagnosis

Junchao Guo[1], Zhanqun Shi[1], Haiyang Li[2,*], Dong Zhen[1,*], Fengshou Gu[2], Andrew. D. Ball[2]

[1]Tianjin Key Laboratory of Power Transmission and Safety Technology for New Energy Vehicles, School of Mechanical Engineering, Hebei University of Technology, Tianjin, 300401, China.

[2]Centre for Efficiency and Performance Engineering, University of Huddersfield, Huddersfield, HD1 3DH, UK.

[*]Corresponding author. E-mail address: Haiyang.Li@hud.ac.uk; d.zhen@hebut.edu.cn.

Abstract

Transient impulses caused by local defects are critical for the fault detection of rotating machines. However, they are extremely weak and overwhelmed in the strong noise and harmonic components, making the transient features are very difficult to be extracted. This paper proposes an adaptive multi-scale improved differential filter (AMIDIF) to enhance the identification of transient impulses for rotating machine fault diagnosis. In this scheme, firstly, the AMIDIF is performed to decompose the measured signal of rotating machine into a series of multi-scale improved differential filter (MIDIF) filtered signals. Subsequently, in view of the MIDIF filtered signals exhibit varying extents of validity in revealing fault features, a weighted reconstruction method using correlation analysis is proposed in which the weighted coefficients are counted and distributed to the corresponding MIDIF filtered signals to highlight the effective MIDIF filtered signals and weaken the invalid ones. Finally, the transient impulse components of rotating machinery are obtained by multiplying the weighted coefficients and the MIDIF filtered signals under different scales. Furthermore, the fault types of rotating machines are inferred from the fault defect frequencies in the envelope spectrum of the transient impulses. Simulation analysis and experimental studies are implemented to verify the performance of the AMIDIF compared with the state-of-the-art methods including spectral kurtosis (SK), multi-scale average combination different morphological filter (ACDIF) and multi-scale morphology gradient product operation (MGPO). The results prove that the AMIDIF has excellent performance in extracting transient features for rotating machines fault diagnosis.

Keywords: Adaptive multi-scale improved differential filter; Weighted coefficients; Correlation coefficients; Rotating machinery; Fault diagnosis

Nomenclature

EMD	Empirical mode decomposition
TQWT	Turntable Q-factor wavelet transform
SR	Stochastic resonance
VMD	Variational mode decomposition
MO	Morphological operator
MF	Morphological filter
CMF	Combination morphological filter
MG	Morphology gradient
DIF	Difference filter
IDIF	Improved differential filter
MDIF	Multi-scale difference filter
CO	Close-open
OC	Open-close
COOC	Difference between the CO and OC
AVG	Average
BTH	Black top hat
MBTH	Multi-scale black top hat
WTH	White top hat
MWTH	Multi-scale white top hat
$\mathrm{AMMG_{DE}}$	Average multi-scale morphological dilate-erode gradient
WAMMG	Weighted average multi-scale morphological gradient
GA	Genetic algorithm
PSO	Particle swarm optimization
FEF	Feature energy factor
FDK	Frequency domain kurtosis
TEK	Teager energy kurtosis
SK	Spectral kurtosis
ACDIF	Average combination different morphological filter
MGPO	Morphology gradient product operation
AMDIF	Adaptive multi-scale differential filter
MIDIF	Multi-scale improved differential filter
WMIDIF	Weighted multi-scale improved differential filter
AMIDIF	Adaptive multi-scale improved differential filter

1. Introduction

Rotating machines are widely applied in the modern industries. After long-term operation, they may have unexpected failures, which will affect the performance and efficiency of other key components or even the entire mechanical transmission system [1-3]. It is critical to monitor the working status of rotating machines to prevent catastrophic failures and reduce severe economic losses. When a local fault occurs, the transient impulses will be produced through the contact between the defect and the mating surface. However, due to strong random noise and harmonic components interference, the transient impulses that reflect the failure mechanism cannot be separated effectively from the measurement signals [4-6]. Therefore, it is vital to eliminate random noise and harmonic components to obtain transient features from the measurement signal for rotating machines condition monitoring and fault detection.

Currently, various advanced signal processing algorithms have been investigated to enhance the weak transient features in the measured signal, such as empirical mode decomposition (EMD), turntable Q-factor wavelet transform (TQWT), stochastic resonance (SR) and variational mode decomposition (VMD), etc. Although these algorithms can effectively diagnose the faults of rotating machines, there are still some limitations in their applications. For instance, the EMD can divide the measured signal into a certain number of intrinsic mode functions (IMFs), but it is governed by the stopping criterion and mode mixing [7-8]. The TQWT is an effective denoising algorithm, but it is affected by Q factor selection [9-10]. The SR has a good performance in obtaining sensitive fault features, but its system parameters will affect the denoising effect [11-12]. The VMD can eliminate the interference parts from random noise and harmonic components to obtain fault features, but it faces the problem of decomposition modes and balance parameters [13-14]. More importantly, these signal processing methods inevitably weaken useful signal details when eliminating background noise, which may affect the accuracy of fault detection.

In contrast, morphological filter (MF) is an excellent nonlinear signal analysis approach that effectively modifies signal details by intersecting with structural element (SE) [15]. With this advantage, MF-based fault detection algorithms have been studied in the last decade [16-18]. For instance, Nikolaou et al. [16] utilized basic morphological operators to obtain impulses and successfully applied them to fault diagnosis. Wang et al. [17] designed a combination morphological filter (CMF) to highlight the impulsive components from the measured signal by eliminating the statistical deviations of the amplitude. Hu et al. [18] proposed an improved morphology gradient (MG), which constructs SE by using harmonic waveforms to extract impulse features from low signal-to-noise ratio (SNR) signals. However, these filters are single-scale morphological analysis methods and their SE scales are fixed, so they may lack integrity when extracting fault features. Aiming at solving the inadequacies of single-scale morphology analysis, a multi-scale morphological analysis method was proposed by Zhang and proved that it is superior to single-scale filters in rotating machines fault diagnosis [19]. Subsequently, Osman et al. [20] developed a multi-scale difference filter (DIF) and Hilbert-Huang transform to discover rolling bearing faults. Raj et al. [21] presented a hybrid algorithm based on multi-scale MG and fuzzy inference for incipient bearing fault detection. Li et al. [22] constructed an improved multi-scale differential filter (COOC), which combines the close-open (CO) filter and the open-close (OC) filter to detect rolling bearing faults. Since the above-mentioned multi-scale morphological filters can only extract positive or negative impulses in a signal at the same time, Dong et al. [23] proposed an average (AVG) filter based on the combination of the closing and opening to obtain bidirectional impulses of the vibration signals. However, the impulse amplitude of AVG is weakened [24]. In view of the multi-scale black top hat (MBTH) represents the difference between the original signal and opening operator and is mainly used

to obtain negative impulses, while the multi-scale white top hat (MWTH) indicates the difference between the closing operator and original signal to extract positive impulses [19, 25], an adaptive multi-scale improved differential filter (AMIDIF) according to the difference between the MBTH and MWTH is proposed to extract cyclic impulses for accurate rotating machinery diagnosis in this study. However, it is still a challenge task to effectively finalize the weighted coefficients in the AMIDIF to improve the accurateness of the transient impulse component extraction.

To solve this issue, a large number of researches have been conducted until now. Li et al. [26] put forward the averaged multi-scale morphological dilate-erode gradient ($\mathrm{AMMG_{DE}}$) filter to detect gear failures, but the weighted coefficients of different SE scales are the identical in the $\mathrm{AMMG_{DE}}$ filter. Subsequently, Li et al. [27] developed the weighted average multi-scale morphological gradient (WAMMG) to extract bearing fault features. In WAMMG, the large scale weighted coefficients can effectively suppress noise, while the detailed impulse information for indicating fault features is retained by the small scale weighted coefficients. Besides, the WAMMG method lacks adaptive abilities. Recently, Li et al. [28] and Deng et al. [29] constructed an adaptive weighted algorithm using the genetic algorithm (GA) and particle swarm optimization (PSO) to determine the weighted coefficients, respectively. Yan et al. [30] and Li et al. [31] put forward using the feature energy factor (FEF) and frequency domain kurtosis (FDK) to calculate the weighted coefficients, respectively. However, the former GA and PSO are affected by the fitness function, while the latter FEF and FDK only consider the fault signal in a single abnormal mode when determining the weighted coefficients and are not compared with the normal signal, so it is extremely difficult to highlight more useful fault components in the final output signal. This paper introduces a novel weighted coefficient algorithm based on the correlation coefficients between the vibration signals collected in abnormal circumstances and its MIDIF filtered signals, and between the MIDIF filtered signals and the vibration signal acquired in normal circumstances. This algorithm can extremely enhance the sensitive fault components and weaken the insensitive ones by removing the common information between the abnormal signal and normal signal. Based on the above considerations, the correlation coefficient method is exploited to optimize the weighted coefficients of the AMIDIF.

To sum up, a novel AMIDIF based on the difference between the MBTH and MWTH is developed for rotating machines fault detection. This method can effectively enhance the transient impulses for extracting fault features from rotating machinery with strong random noise and harmonic components. The main contributions and innovations of the paper can be summarized into two aspects: (1) AMIDIF is able to obtain bidirectional impulses in the vibration signals to enhance the fault feature extraction and suppress background noise. (2) A weighted reconstruction algorithm based on correlation analysis is presented, in which the calculation of weight coefficients can effectively highlight the useful MIDIF filtered signals and reduce invalid ones. The performance of the AMIDIF is analyzed through a numerical simulation and experimental cases, and its effectiveness is validated by comparison with the existing algorithms.

The paper is organized in 7 sections. After the introduction, Section 2 investigates the theoretical basis of the improved differential filter (IDIF), and the merits of IDIF over other morphological filters are investigated in accordance with the simulation analysis. Section 3 presents the AMIDIF scheme according to correlation analysis. In Section 4, the diagnostic process of the AMIDIF is thorough. And the AMIDIF is tested by a numerical simulation in Section 5. Two experimental case researches on support bearing with outer race fault and planetary gearbox with sun gear chipping are provided in Section 6. And the conclusions are drawn in Section 7.

2. Improved differential filter

2.1. IDIF

The mathematical morphology (MM) was firstly presented as an image processing methodology by Matheron and Serra [32]. Assuming that the input sequence $f(n)$ and selected SE $g(m)$ are discrete signal over a domain of $F = (0,1,\dots,N-1)$ and $G = (0,1,\dots,M-1)$ $(M \le N)$, respectively. The dilation and erosion are expressed as:

$$(f \oplus g)(n) = \max[f(n-m) + g(m)], \quad m \in 0,1,\cdots,M-1$$

(1)

$$(f \Theta g)(n) = \min[f(n+m) - g(m)], \quad m \in 0,1,\cdots,M-1$$

(2)

where $\oplus$ and Θ are the dilation and erosion operations, respectively. The erosion operator can remove the positive impulses and smooth the negative ones. By comparison, the dilation operator can reduce the negative impulses and smooth the positive ones. The morphology gradient (MG) is expressed as the difference between the erosion and dilation:

$$MG(f(n)) = (f \oplus g)(n) - (f \Theta g)(n) \tag{3}$$

The opening and closing operators can be generated by cascading the dilation and erosion operators, which can be formulated as:

$$(f \circ g)(n) = (f \Theta g \oplus g)(n) \tag{4}$$

$$(f \bullet g)(n) = (f \oplus g \Theta g)(n) \tag{5}$$

where $\circ$ and $\bullet$ indicate the opening and closing operators, respectively. The opening operator reduces the positive impulses and preserves the negative ones, while the closing operator preserves the positive impulses and removes the negative ones. The difference filter (DIF) is expressed as the difference between the closing and opening:

$$DIF(f(n)) = (f \bullet g)(n) - (f \circ g)(n) = [(f \bullet g)(n) - f(n)] + [f(n) - (f \circ g)(n)] \tag{6}$$

where $(f \bullet g)(n) - f(n)$ and $f(n) - (f \circ g)(n)$ represent the black top-hat (BTH) and white top-hat (WTH), respectively. The former is applied to extract negative impulses, while the latter is utilized to obtain positive impulses. Considering the presence of bidirectional impulses in the original signal, the improved differential filter (IDIF) based on the BTH and WTH is formulated as:

$$IDIF(f(n)) = WTH(n) - BTH(n) = 2f(n) - (f \circ g)(n) - (f \bullet g)(n) \tag{7}$$

2.2. Simulation analysis

A simulation signal $x(t) = \sin(10\pi t) + n(t)$ is analyzed and compared with the different morphological filters to evaluate the performance of IDIF. The sampling frequency of the $x(t)$ is 1024 Hz and signal samples are 1024. And $n(t)$ denotes a certain number of positive and negative impulses (the interval of the same impulse is 400 sampling points) with amplitude of 1. Hereafter, the four basic morphological operators (MOs) using the flat SE with the length of L=10 are exploited to analyze the

simulation signal as presented in Fig. 1.

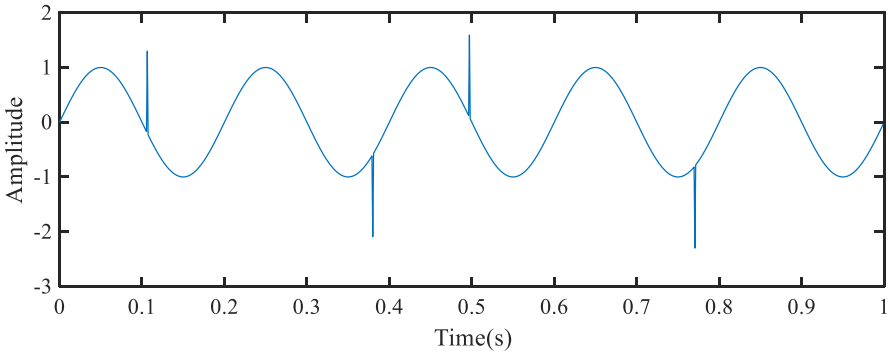

Fig. 1. Waveform of the simulation signal.

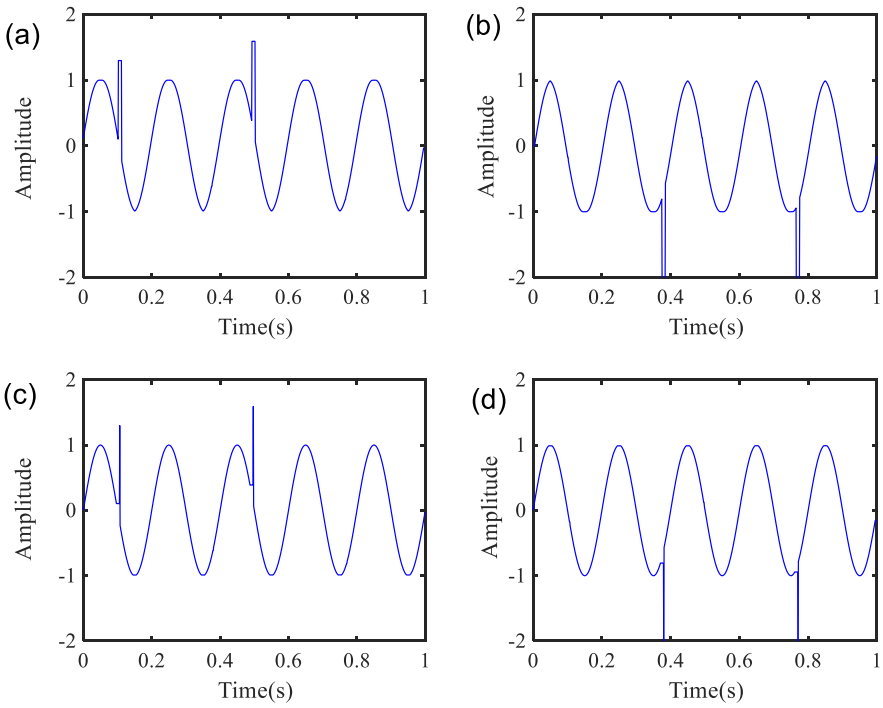

Fig. 2. Processing results by the basic MOs: (a) dilation (b) erosion (c) closing (d) opening.

Fig. 2 displays the processing results by the four basic MOs. However, the MOs can only extract positive or negative impulses, but cannot obtain bidirectional impulses. Subsequently, the different MFs (i.e. MG, AVG, DIF, COOC, BTH, WTH and IDIF) are exploited to handle the signal as illustrated in Fig. 1. The results of the different MFs are depicted in Fig. 3. It can be found that the MG, DIF and COOC can extract impulses, but all negative impulses are transformed into positive impulses. Although the AVG can obtain positive and negative impulses, the amplitude of the extracted impulses is weakened. The WTH can only extract positive impulses, while the BTH can extract negative impulses. And the BTH extracts a negative impulse that is converted into a positive impulse. The processing result of the IDIF is shown in Fig. 3(g), which is capable of obtaining the bidirectional impulses. Therefore, it is verified that the IDIF is more effective for extracting cyclic impulses.

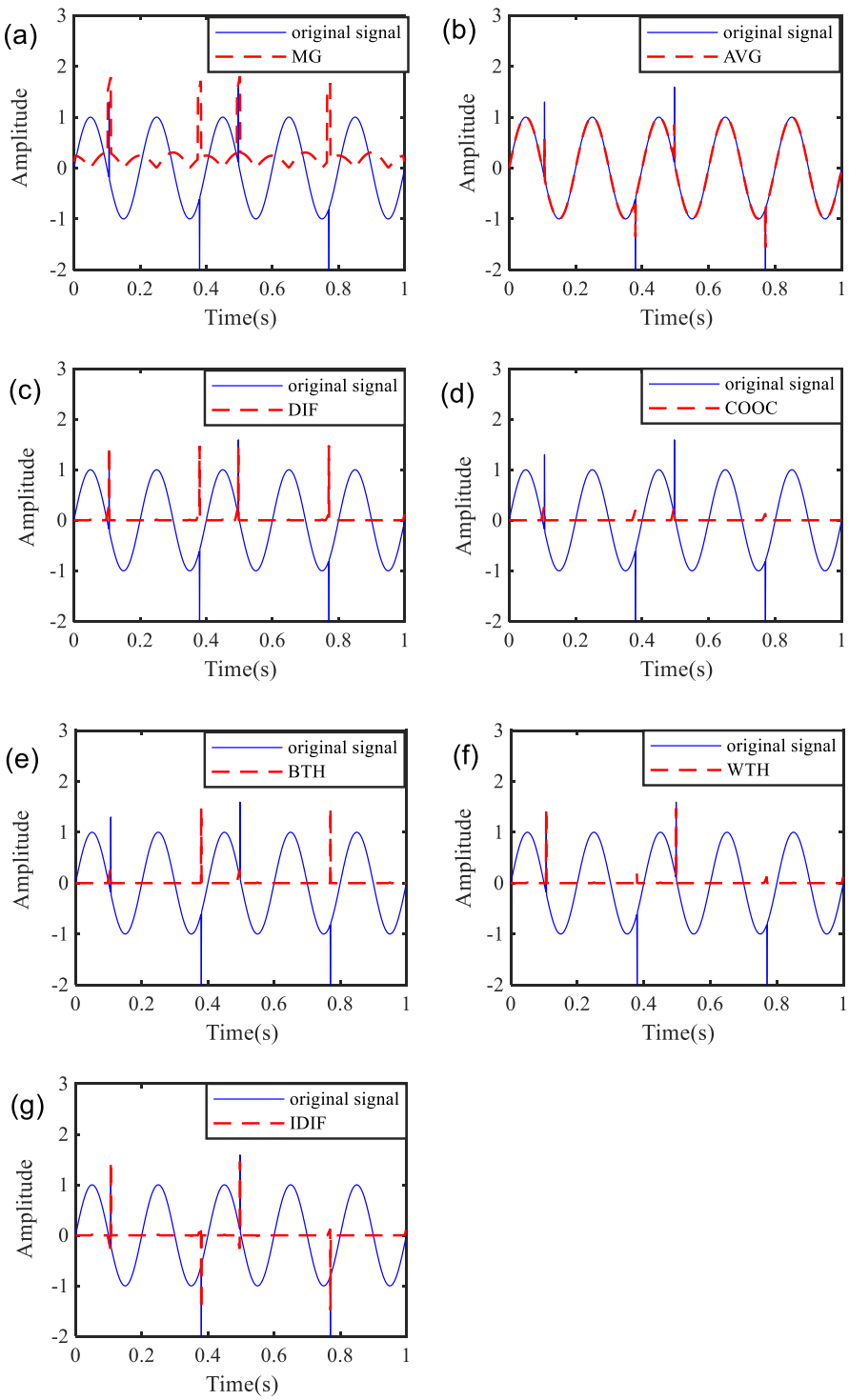

Fig. 3. Processing results by the MFs: (a) MG (b) AVG (c) DIF (d) COOC (e) BTH (f) WTH (g) IDIF.

3. Adaptive multi-scale improved differential filter

3.1. MIDIF

To mine fault features more accurately, multi-scale methods have been carried out in Ref [33-35]. Suppose g is a unit SE, and ε $(\varepsilon = 1,2,\ldots,k)$ is the scale, the SE used in the scale ε can be expressed

as:

$$\varepsilon g = \underbrace{g \oplus g \oplus \cdots \oplus g}_{\varepsilon-1\ times} = \underbrace{((g \oplus \cdots \oplus g) \oplus g) \oplus g}_{\varepsilon-1\ times} \tag{8}$$

Multi-scale basic morphological operators can be given as:

$$(f \oplus \varepsilon g)(n) = f \oplus \underbrace{(g \oplus g \oplus \cdots \oplus g)}_{\varepsilon-1\ times} \tag{9}$$

$$(f \Theta \varepsilon g)(n) = f \Theta \underbrace{(g \Theta \mathrm{g} \Theta \cdots \Theta g)}_{\varepsilon-1\ times} \tag{10}$$

$$(f \mathrm{o} \varepsilon g)(n) = \big((f \Theta \varepsilon g) \oplus \varepsilon g\big)(n) \tag{11}$$

$$(f \bullet \varepsilon g)(n) = \big((f \oplus \varepsilon g) \Theta \varepsilon g\big)(n) \tag{12}$$

Subsequently, the multi-scale black top-hat (MBTH) and multi-scale white top-hat (MWTH) are further defined as:

$$MBTH\big(f(n)_{\varepsilon g}\big) = (f \bullet \varepsilon g)(n) - f(n) \tag{13}$$

$$MWTH\big(f(n)_{\varepsilon g}\big) = f(n) - (f \mathrm{o} \varepsilon g)(n) \tag{14}$$

Correspondingly, the MBTH is used to extract negative impulses, while the MWTH is applied to obtain positive impulses. Considering the presence of bidirectional impulses in the original signal, the multi-scale improved differential filter (MIDIF) can be expressed as:

$$MIDIF(f(n)_{\varepsilon g}) = MWTH\big(f(n)_{\varepsilon g}\big) - MBTH\big(f(n)_{\varepsilon g}\big) = 2f(n) - (f \mathrm{o} \varepsilon g)(n) - (f \bullet \varepsilon g)(n) \tag{15}$$

3.2. Adaptive weighted average

Considering that large scales can suppress the background noise, but may destroy useful signal details, while small scales can smooth signal geometric characteristics, but may not effectively inhibit noise. Many researchers use the weighted average of MF as the final output [29-30]:

$$MIDIF(f(n)) = \sum_{\varepsilon=1}^{\varepsilon_{\max}} (\omega_\varepsilon \cdot MIDIF(f(n)_{\varepsilon g})) \tag{16}$$

where ω_ε is the weighted coefficients under different scales $\varepsilon(\varepsilon = 1,2,\ldots,\varepsilon_{max})$, which will influence the processing results of MIDIF. Consequently, it is necessary to develop a significant scheme to determine the weighted coefficients ω_ε so that more useful fault components are highlighted in the final output signal. This paper presents a novel weighted coefficient algorithm via the correlation coefficients [36-37] to determine the weighted coefficients ω_ε, and the specific procedure is summarized as follows:

Step 1: Define the input signal $f(n)$ in SE as the normal circumstances signal, and $\hat{f}(n)$ as the abnormal circumstances signal.

Step 2: Calculate the correlation coefficient u_ε between the abnormal circumstances signal $\hat{f}(n)$ and filtered signal $MIDIF(\hat{f}(n)_{\varepsilon g})$ of each scale, which can be defined as:

$$u_\varepsilon = \frac{\sum_{n=0}^{N-1}(\hat{f}(n)-\bar{\hat{f}})(MIDIF(\hat{f}(n)_{\varepsilon g})-\overline{MIDIF(\hat{f})})}{\sqrt{\sum_{n=0}^{N-1}(\hat{f}(n)-\bar{\hat{f}})^2 \sum_{n=0}^{N-1}(MIDIF(\hat{f}(n)_{\varepsilon g})-\overline{MIDIF(\hat{f})})^2}} \tag{17}$$

where $\bar{\hat{f}}$ and $\overline{MIDIF(\hat{f})}$ present the mean values of $\hat{f}(n)$ and $MIDIF(\hat{f}(n)_{\varepsilon g})$, respectively.

Step 3: Calculate the correlation coefficient φ_ε between the normal circumstances signal $f(n)$ and filtered signal $MIDIF(f(n)_{\varepsilon g})$ of each scale, which can be defined as:

$$\varphi_\varepsilon = \frac{\sum_{n=0}^{N-1}(f(n)-\bar{f})(MIDIF(f(n)_{\varepsilon g})-\overline{MIDIF(f)})}{\sqrt{\sum_{n=0}^{N-1}(f(n)-\bar{f})^2 \sum_{n=0}^{N-1}(MIDIF(f(n)_{\varepsilon g})-\overline{MIDIF(f)})^2}} \tag{18}$$

where $\bar{f}$ and $\overline{MIDIF(f)}$ denote the mean values of $f(n)$ and $MIDIF(f(n)_{\varepsilon g})$, respectively.

Step 4: Calculate the fault-related coefficient η_ε:

$$\eta_\varepsilon = u_\varepsilon - \varphi_\varepsilon \tag{19}$$

Step 5: Calculate the weighted coefficients ω_ε of each scale ε:

$$\omega_\varepsilon = \eta_\varepsilon / \sum_{\varepsilon=1}^{\varepsilon_{max}} \eta_\varepsilon \tag{20}$$

4. Diagnostic process of AMIDIF

In this subsection, an AMIDIF method is developed for rotating machines fault detection. The specific diagnostic process is presented in Fig. 4, and the comprehensive contents are introduced as below:

Step 1: Perform AMIDIF on the measurement signals of rotating machines to generate a series of MIDIF filtered signals.

Step 2: Determine the scale range of the AMIDIF; the scales range from 1 to $[f_s/f_o] - 2$, with the increases of 1, where f_s and f_o indicate the sampling frequency and fault characteristic frequency, respectively.

Step 3: Calculate the correlation coefficient between the vibration signal collected in abnormal circumstances and its MIDIF filtered signals, and between the MIDIF filtered signals and the vibration signal acquired in normal circumstances.

Step 4: Calculate the fault-related coefficients by subtracting the correlation coefficients of the above two circumstances.

Step 5: Calculate the weighted coefficients by normalizing the fault-related coefficients under different scales.

Step 6: Acquire the AMIDIF filtered signal by multiplying the weighted coefficients and MIDIF filtered signals in abnormal circumstances.

Step 7: Obtain the envelope spectrum of the AMIDIF filtered signal to identify the rotating machinery faults.

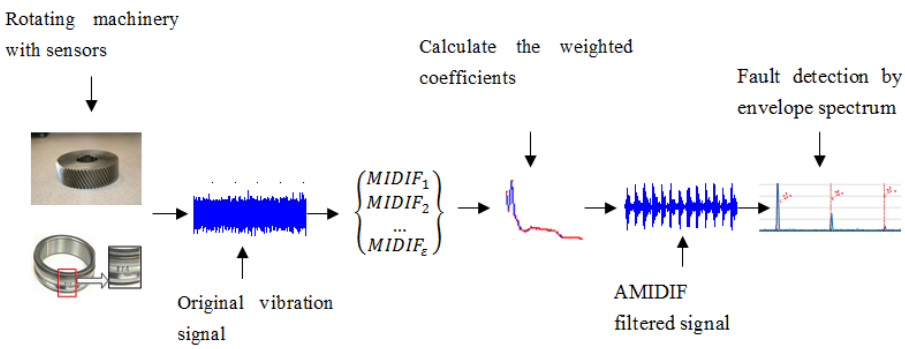

Fig. 4. The flowchart of the AMIDIF method.

5. Simulation validation

5.1. Simulation model

In this section, a numerical simulation signal is designed to elaborate the performance of the AMIDIF in extracting fault features. When a local fault occurs in a rolling bearing, its vibration form is constantly expressed as periodic impulses. However, the transient impulses are inevitably overwhelmed by random noise and harmonic components. To simulate the actual signal of rolling element bearing, the

bearing fault model is defined as follows [38-39]:

$$x(t) = s(t) + b(t) + h(t) + n(t) \tag{21}$$

where $s(t)$ indicates the periodic impulse component caused by rolling element bearing defect, and its model is formulated as [40]:

$$s(t) = \sum_{j=1}^{J} B_j \exp[-\beta(t - jT - \tau_r)]\sin(2\pi f_c(t - jT - \tau_r)) \tag{22}$$

where J indicates the number of periodic impulse, B_j stands the amplitude of the jth periodic impulse, T represents the impulse interval, f_c is the resonant frequency, set to 600 Hz, β stands the decay parameter, set to 110, and τ_r indicates a small random slippage variable of the rolling elements, which is often expressed as $1\%\sim2\%$ of the impulse interval T. The $b(t)$ represents random impulse aroused by external interference from the bearing housing, and its model can be defined as [41]:

$$b(t) = \sum_{j=1}^{M} A_j \exp[-\alpha(t - jT)]\sin(2\pi f_d(t - jT)) \tag{23}$$

where M and A_j indicate the number of random impulses and the amplitude of the jth random impulse, f_d denotes the resonant frequency, equal to 200 Hz, α represents the decay parameter, set to 35. The $h(t)$ is employed to simulate harmonic components, and its model is formulated as:

$$h(t) = 0.2\sin(2\pi f_1 t) + 0.1\ \sin(2\pi f_2 t) \tag{24}$$

where f_1 and f_2 are set to 20 Hz and 50 Hz, respectively. Meanwhile, the sampling frequency is 2048 Hz and data length is 8192, $f_o = 1/T$ represents the fault defect frequency, equal to 32 Hz. The $n(t)$ is Gaussian white noise. Fig. 5 presents the periodic impulse, random impulse, Gaussian white noise, harmonic component and composite signal, respectively. Fig. 6(a) and Fig. 6(b) describe the spectrum and envelope spectrum of the composite signal at a signal-to-noise ratio (SNR) of -5 dB. From the frequency spectrum, the two interference frequencies (f_1 and f_2) are presented clearly, but the fault defect frequency f_o and its harmonics (i.e. $2f_o, 3f_o, 4f_o, 5f_o$ and $6f_o$) cannot be observed. As depicted in Fig. 6(c), only the first two fault defect frequencies (i.e. f_o and $2f_o$) can be found, the higher order harmonics (i.e. $3f_o, 4f_o, 5f_o$ and $6f_o$) cannot be identified.

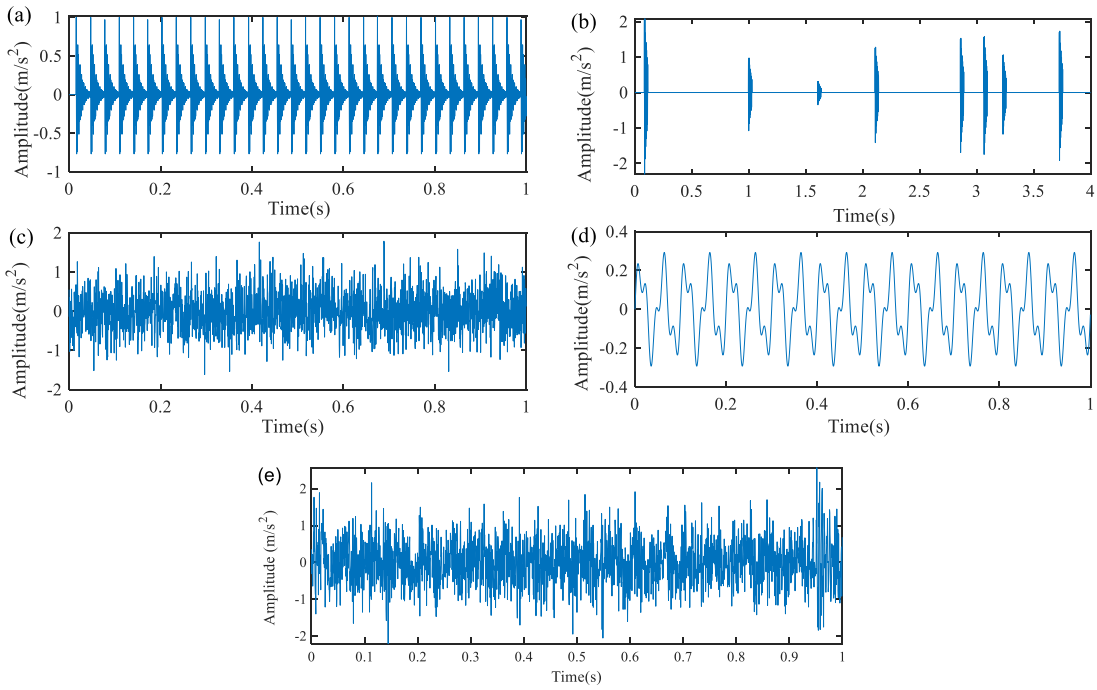

Fig. 5. (a) periodic impulse (b) random impulse (c) Gaussian white noise (d) harmonic component (e) composite signal.

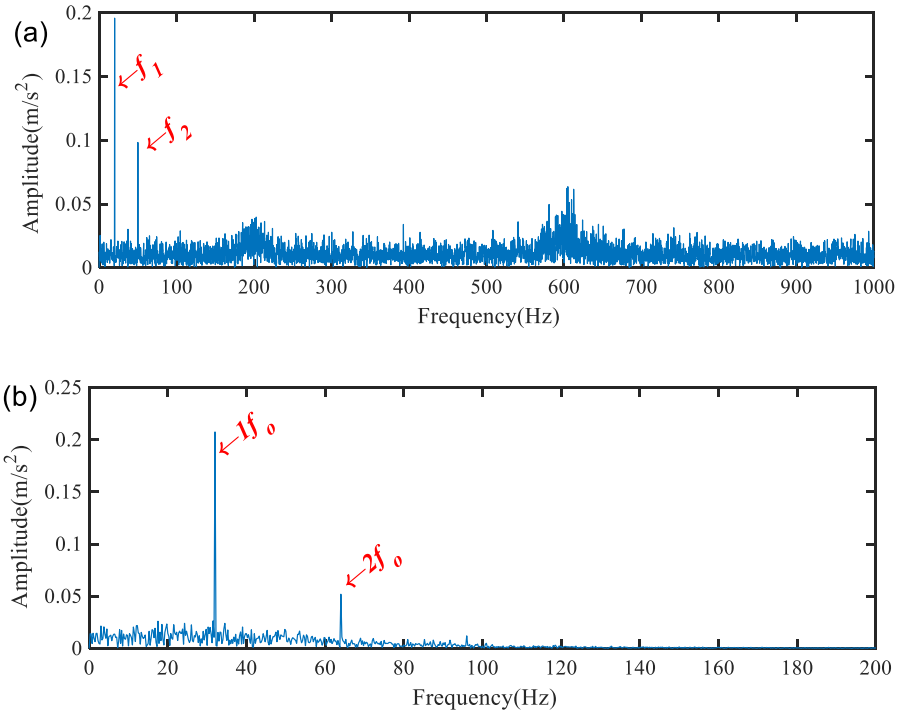

Fig. 6. Simulated bearing signal: (a) spectrum (b) envelope spectrum with central frequency of 600 Hz and a bandwidth of 100Hz.

To accurately extract the fault defect frequency f_o and its harmonics, the AMIDIF is exploited to handle the composite signal as illustrated in Fig. 5(e). Firstly, the composite signal is decomposed into a series of MIDIFs using the AMIDIF. The correlation coefficients between the composite signal collected under abnormal or normal circumstances and the MIDIFs under different scales are calculated. Subsequently, the fault-related coefficients are calculated by the difference between the abnormal signal and normal signal to remove common information to highlight the fault component of the simulated bearing. To demonstrate the advantages of the AMIDIF, an adaptive multi-scale difference filter (AMDIF) [18] based on correlation coefficient is considered for the simulation signal. Finally, the weighted coefficients of the AMIDIF and AMDIF are calculated by normalizing the fault-related coefficients of different scales. The weighted coefficient with different scales of SE is displayed in Fig. 7. The results of the AMIDIF and AMDIF are presented in Fig. 8 and Fig. 9, respectively. As can be clearly observed from Fig. 8, the fault defect frequency f_o and its harmonics (i.e. $2f_o, 3f_o, 4f_o, 5f_o$ and $6f_o$) of the simulated signal are obvious. In contrast, the first three fault characteristic frequencies (i.e. f_o, $2f_o$ and $3f_o$) can be identified, and there are still abundant interference frequencies in the low frequency band in Fig. 9. This means that the AMIDIF can more efficiently obtain the fault defect frequencies than the AMDIF.

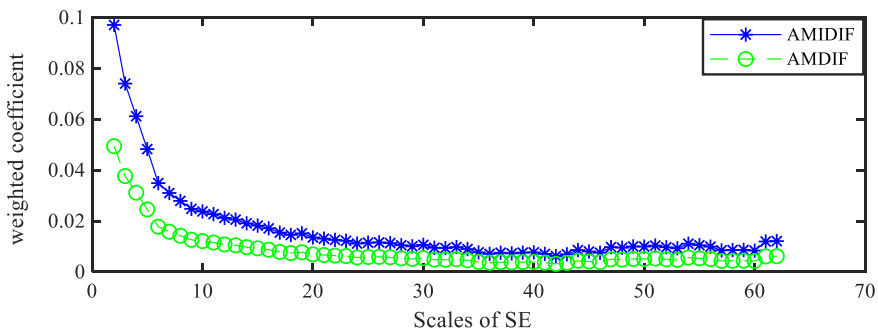

Fig. 7. The weighted coefficient with different scales of SE based on correlation coefficient.

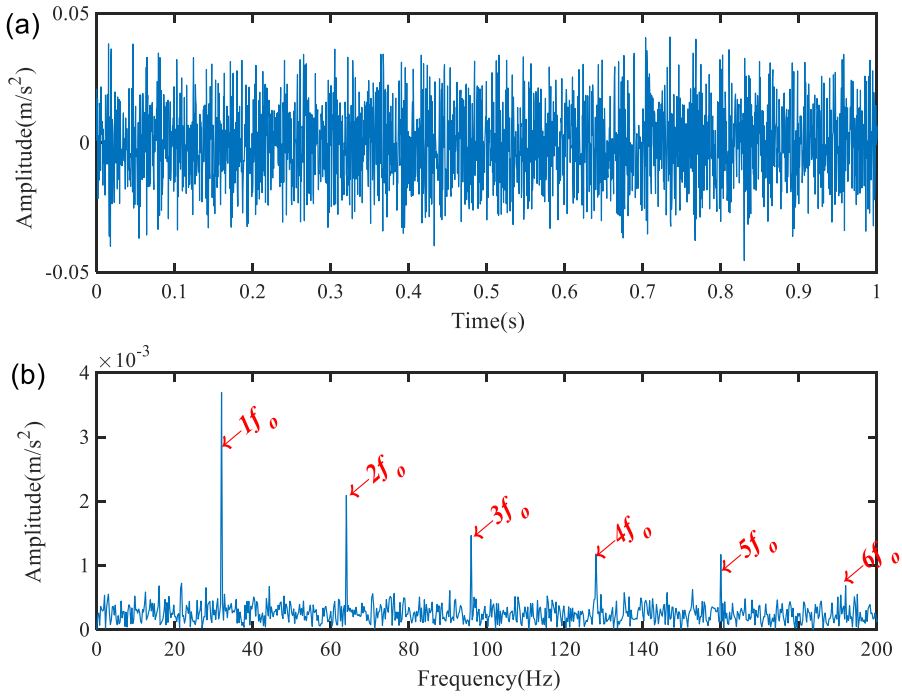

Fig. 8. Processing results of the simulated bearing signal by the AMIDIF: (a) waveform (b) envelope spectrum.

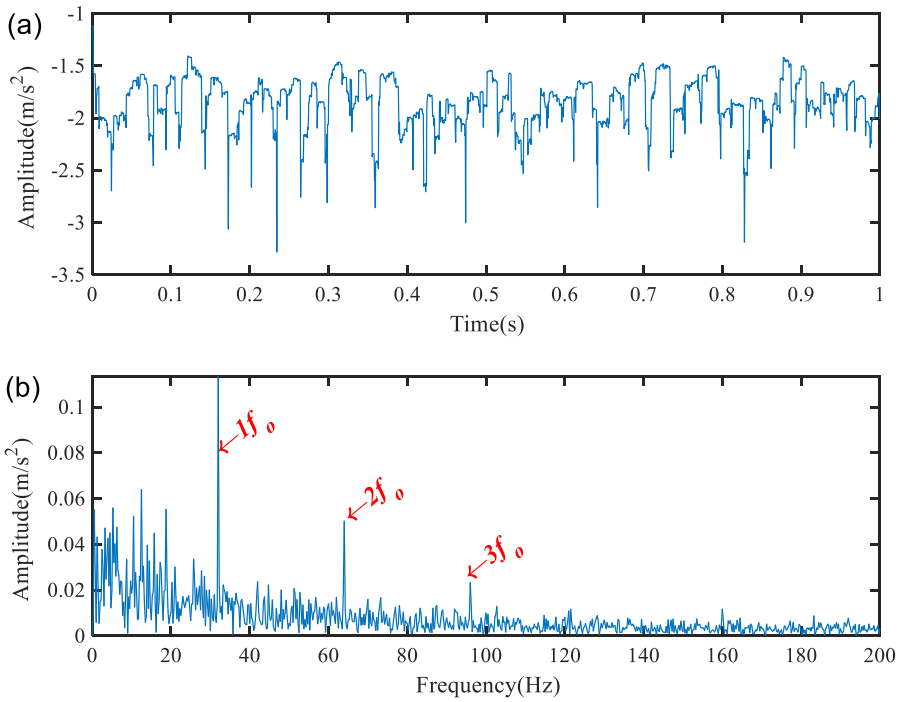

Fig. 9. Processing results of the simulated bearing signal by the AMDIF: (a) waveform (b) envelope spectrum.

5.2. Comparison with multi-scale difference morphology filters

To demonstrate the advantages of the AMIDIF, the multi-scale average combination different

morphological filter (ACDIF) [42] and multi-scale morphology gradient product operation (MGPO) [43] methods are utilized to handle the composite signals presented in Fig. 5(e). According to the literature [42], the multi-scale ACDIF is composed of an average weighted combination of two basic cascade operations, which apply a flat SE to extract impulses from background noise and interference components. The weighted coefficient with different scales of SE based on Teager energy kurtosis (TEK) is depicted in Fig. 10. The multi-scale ACDIF filtered signal is obtained by multiplying the weighted coefficients and ACDIF signals under different scales, and corresponding envelope spectrum are presented in Fig. 11. Only the fault defect frequencies f_o can be found from the Fig. 11(b), the higher order harmonics (i.e. $2f_o$, $3f_o, 4f_o, 5f_o$ and $6f_o$) cannot be identified and interference harmonics are doped in the low frequency band. According to the literature [43], the multi-scale MGPO is formed by the product of two gradient operations (MG and COOC), which uses a flat SE to extract impulses of composite signal. The weighted coefficient with different scales of SE based on feature energy factor (FEF) is depicted in Fig. 12. The multi-scale MGPO filtered signal is calculated by multiplying the weighted coefficients and MGPO signals under different scales, and its envelope spectrum are depicted in Fig. 13. Although the fault defect frequency f_o and its harmonics (i.e. $2f_o$ and $3f_o$) can be identified, there are still some harmonic interference frequencies as plotted in Fig. 13(b). Thus, the simulation results reveal that the AMIDIF is superior to the ACDIF and MGPO.

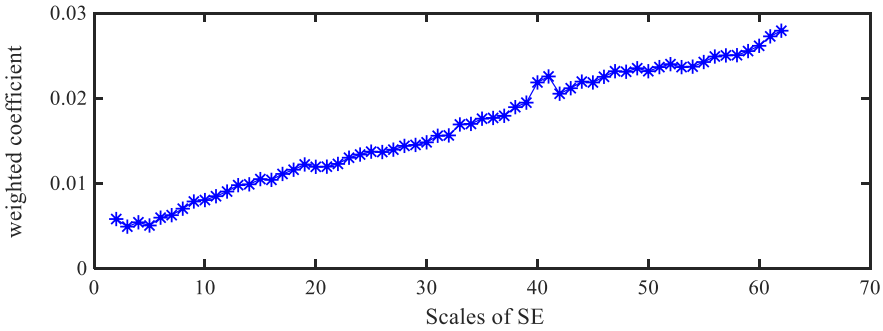

Fig. 10. The weighted coefficient with different scales of SE based on TEK.

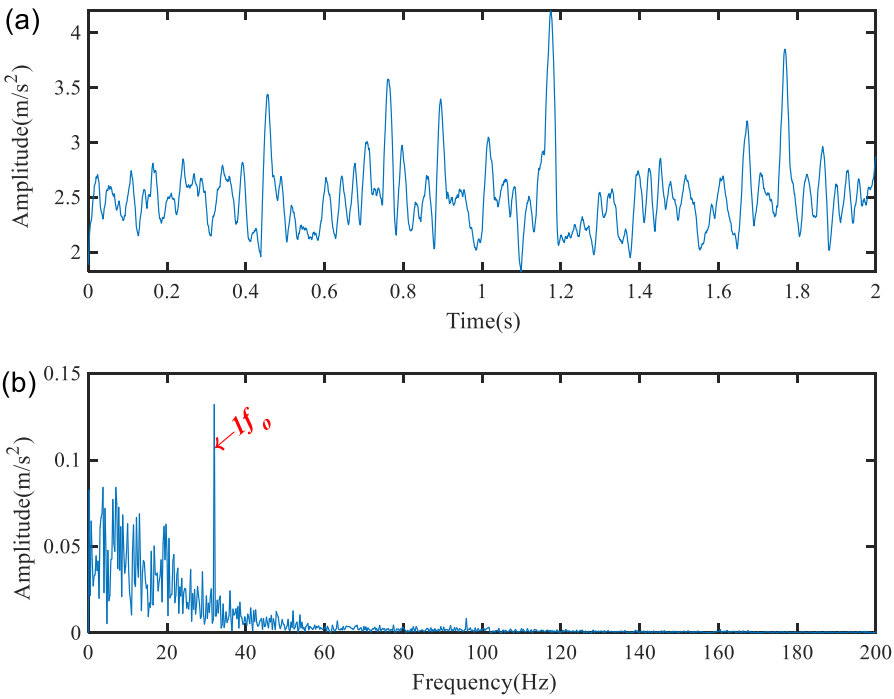

Fig. 11. Processing results of the simulated bearing signal by the ACDIF: (a) waveform (b) envelope spectrum.

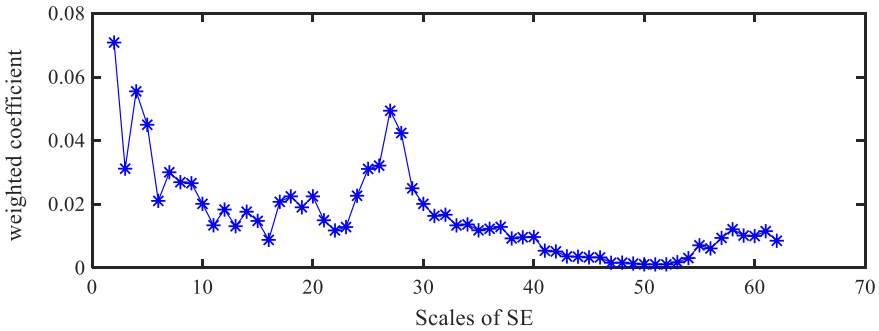

Fig. 12. The weighted coefficient with different scales of SE based on FEF.

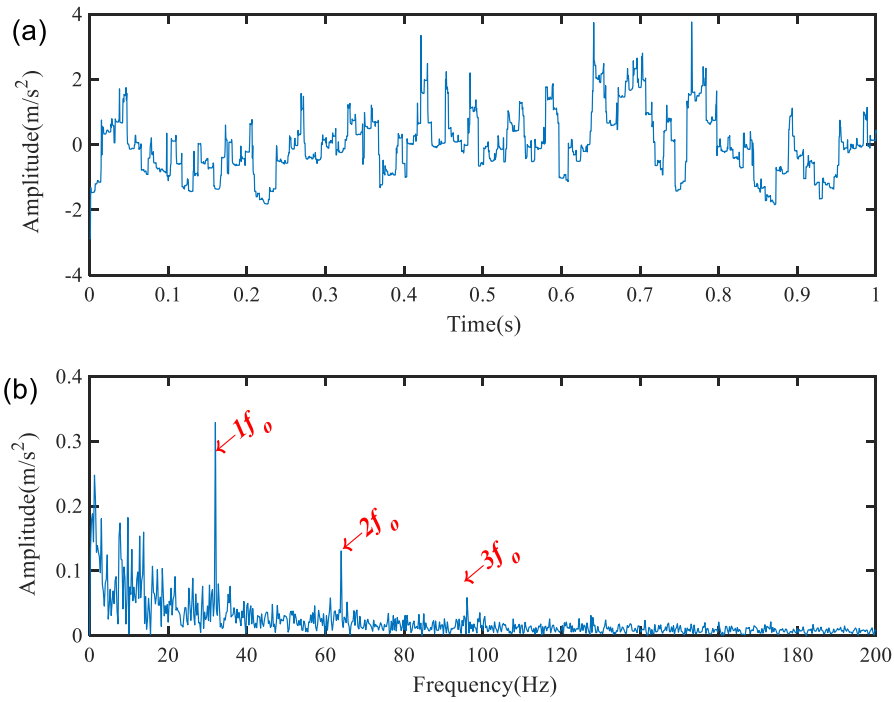

Fig. 13. Processing results of the simulated bearing signal by the MGPO: (a) waveform (b) envelope spectrum.

5.3. Comparison with the SK and MOMEDA algorithm

The spectral kurtosis (SK) put forward by Antoni [44] is the benchmark algorithm for fault detection of rotating machines, so FK is further utilized to analyze the simulation signal. The detection results of the SK are depicted in Fig. 14. It can be noticed that the bandwidth and central frequency of the band pass filter are 341.3 Hz and 170.67 Hz in Fig. 14(a). The envelope and squared envelope spectrum of the filtered signal by the SK are drawn in Fig. 14(b) and (c). From Fig. 14(c), the fault defect frequencies (i.e. $f_o, 2f_o, 3f_o, 4f_o, 5f_o$ and $6f_o$) are identified, but the background noise and the interference frequency components are much larger than those in Fig. 8. The multipoint optimal minimum entropy deconvolution adjusted (MOMEDA) is a new algorithm presented recently in Ref. [45], which has been successfully used for rotating machinery fault diagnosis. Therefore, the above-mentioned simulation signal is analyzed using the MOMEDA for comparison. In the MOMEDA algorithm, the window

function w is a rectangular window whose length is set to 3 and the filter length of L is set to 50 [46-47]. The corresponding diagnosis results obtained using the MOMEDA are depicted in Fig. 15. As depicted in Fig. 15(b), the fault defect frequency f_o and its harmonics (i.e. $2f_o, 3f_o, 4f_o, 5f_o$ and $6f_o$) are identified. To further compare the performance of the five methods (AMIDIF, ACDIF, MGPO, SK and MOMEDA), the signal-to-noise ratio (SNR) and CPU running time are considered in this study. The Intel Core i7 8550U 1.99 GHz CPU with 16.00 GB RAM is used to carry out the simulation. The SNR is expressed as follows [48]:

$$SNR = 10log10\left(\frac{\sum_{i=1}^{N} x^2(i)}{\sum_{i=1}^{N}(x(i)-\hat{x}(i))^2}\right) \tag{25}$$

where $x(i)$ $(i = 1,2,\cdots,N)$ presents the raw signal and $\hat{x}(i)$ indicates the filtered signal, respectively. The contrast results of the five methods (AMIDIF, ACDIF, MGPO, SK and MOMEDA) are shown in Table 1. It can be found that the AMIDIF has the maximum SNR, which indicates that it has a good denoising effect. In addition, the AMIDIF has less CPU running time than the ACDIF and MGPO, but more than the SK and MOMEDA. Here are some explanations about the computational efficiency of the AMIDIF is lower than the SK and MOMEDA. Firstly, the SE scale of the AMIDIF is too large, which will directly increase the weighted coefficients under different scales to increase the number of cycles. Secondly, the weighted coefficients of the AMIDIF need to be performed in two modes, while the SK and MOMEDA algorithms only require a single abnormal mode and only cycle once when processing the signals. Consequently, the analysis results illustrate that the AMIDIF is more capable of accurately extracting impulse features than other four methods in this case.

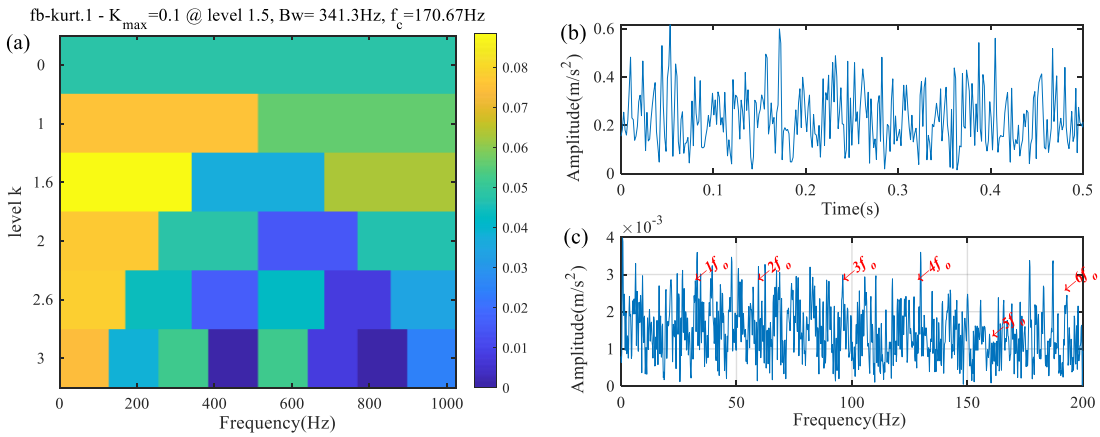

Fig. 14. Processing results of the simulated bearing signal by the SK: (a) kurtogram (b) envelope (c) squared envelope spectrum.

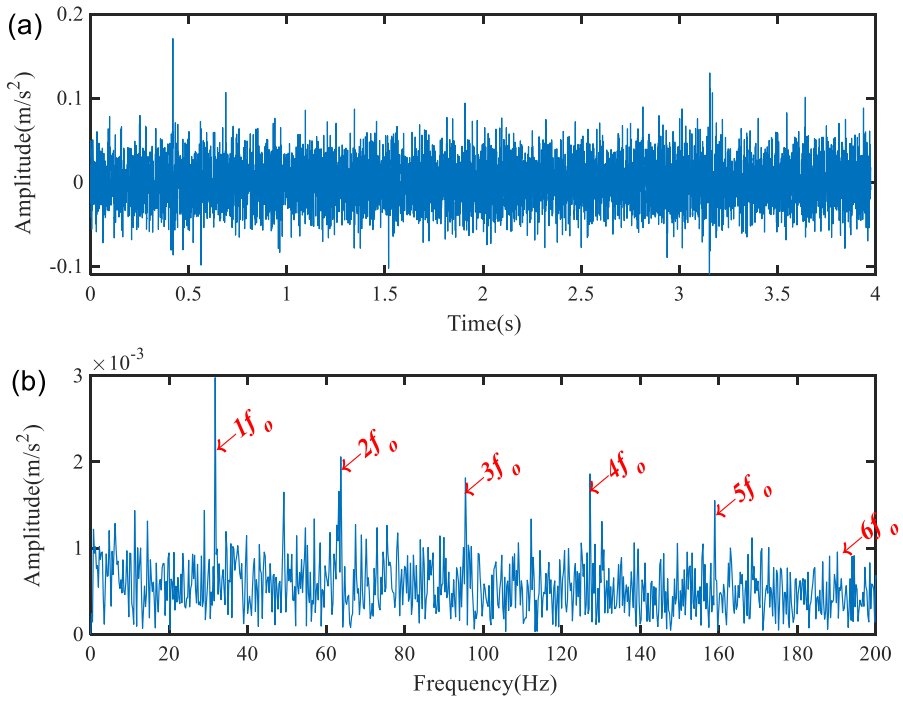

Fig. 15. Processing results of the simulated bearing signal by the MOMEDA: (a) waveform (b) envelope spectrum.

Table 1. The contrast results between the AMIDIF and other four algorithms.

Algorithms	SNR	CPU running time (s)
AMIDIF	0.221	4.976
ACDIF	-12.999	9.828
MGPO	-4.690	9.469
SK	-0.277	3.510
MOMEDA	-0.015	1.747

A good transient impulse extraction algorithm cannot be affected by random noise. Thus, the performance of the AMIDIF under different noise scales is studied. The fault defect index is an evaluation method that has been proven to be efficient in extracting fault features [49]. Given this, the fault defect index is utilized to assess the performance of the AMIDIF under different noise scales in this study. For a given fault defect frequency f, the fault defect index $\bar{\alpha}$ can be defined as follows:

$$\begin{cases} \bar{\alpha} = \dfrac{\alpha(f) + \alpha(2f) + \alpha(3f)}{3} \\ \alpha(f) = \dfrac{A(f)}{\mathrm{mean}(A(f-10), A(f+10))} \end{cases} \tag{26}$$

where $A(f)$ indicates the envelope spectrum amplitude of the fault defect frequency. The fault defect index of the AMIDIF, SK, MOMEDA and narrowband-based envelope spectrum under different noise scales is exhibited in Fig. 16. It can be found that the AMIDIF has stronger fault diagnosis capability than the other three algorithms under different noise scales.

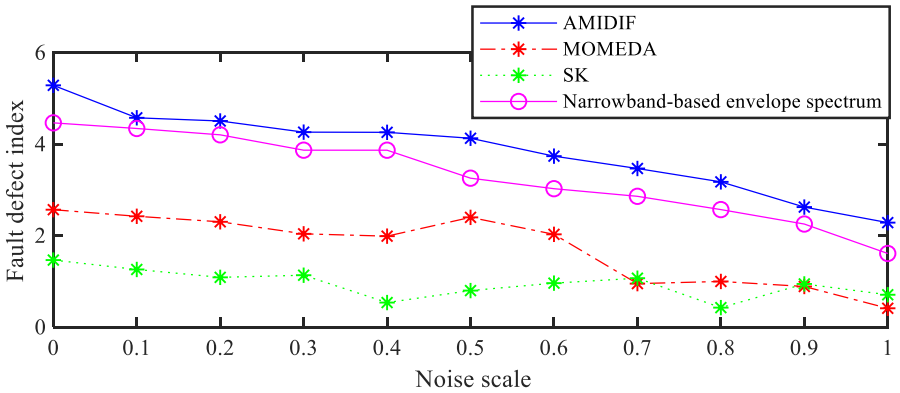

Fig. 16. Fault defect index of the four algorithms under different noise scales.

5.4. Effect of the weighted coefficients on the AMIDIF

To illustrate the effect of the weighted coefficients on the AMIDIF, the traditional multi-scale improved differential filter (MIDIF) and the weighted multi-scale improved differential filter (WMIDIF) are exploited to handle the same signal depicted in Fig. 5(e). The WMIDIF filtered signal is calculated by directly multiplying the weighted coefficients and the MIDIF filtered signals under different scales, as illustrated in Fig. 17. As can be found from Fig. 17(b), the fault defect frequency f_o and its harmonics (i.e. $2f_o, 3f_o, 4f_o, 5f_o$ and $6f_o$) can be distinctly identified, but the interference frequencies are still around the higher order harmonics. The traditional MIDIF is formed by directly averaging all scales IDIF filtered signals. The results of the traditional MIDIF are presented in Fig. 18. Although the fault defect frequency f_o and its harmonics (i.e. $2f_o, 3f_o, 4f_o, 5f_o$ and $6f_o$) can be observed, the amplitude of the interference frequencies is distinctly higher than the amplitude of the fault defect frequencies. By contrast, it can be concluded that the weighted coefficient obtained by the correlation coefficient method can better highlight the useful fault component of the measured signal. In conclusion, by the comprehensive comparative study of the simulated signals, the results prove that the AMIDIF based on correlation coefficient is more suitable and effective in fault diagnosis.

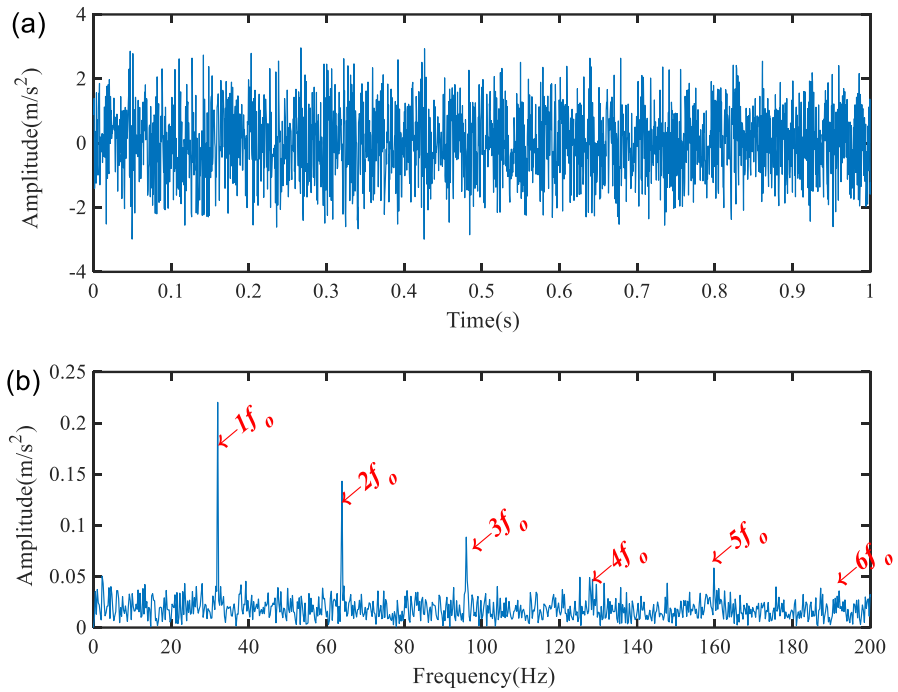

Fig. 17. Processing results of the simulated bearing signal by the WMIDIF: (a) waveform (b) envelope spectrum.

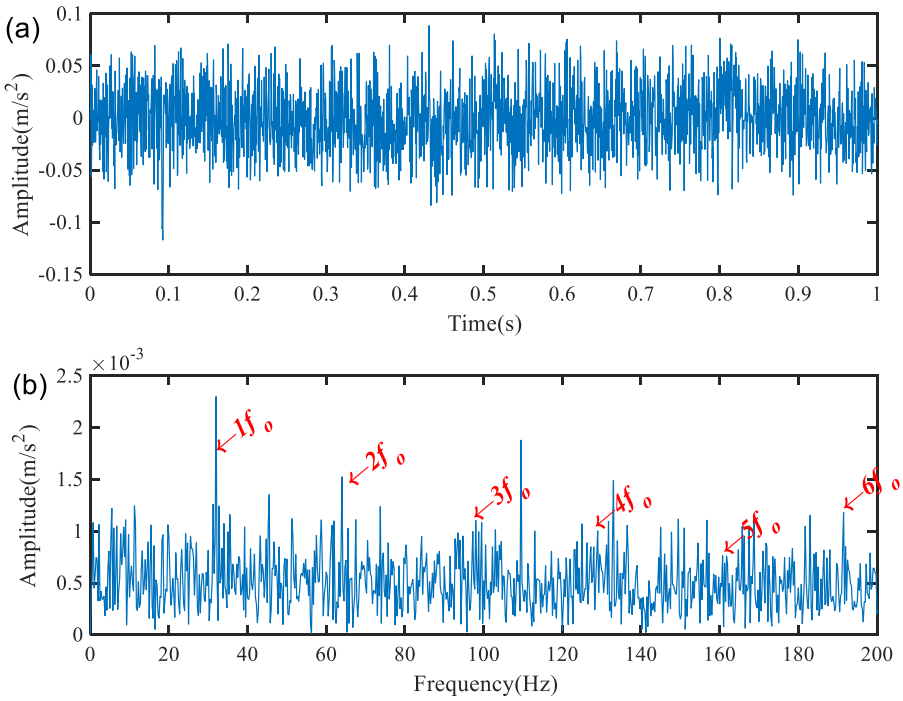

Fig. 18. Processing results of the simulated bearing signal by the MIDIF: (a) waveform (b) envelope spectrum.

6. Experimental verification

To verify the performance of the AMIDIF in fault diagnosis of rotating machines, the experimental cases from rolling element bearing and planetary gearbox are analyzed. Moreover, the effectiveness of

the AMIDIF is contrasted with two multi-scale difference morphology filters (i.e. ACDIF and MGPO), SK and MOMEDA algorithms.

6.1. Case 1: rolling element bearing fault diagnosis

6.1.1. Test setup and data collection

The experimental data is obtained from the bearing test platform as displayed in Fig. 19. It comprises an induction motor, three couplings, two bearing houses and a DC generator. The accelerometer sensor was erected in the bearing housing. An artificial fault (depth 0.3 mm and width 0.1 mm) is emerged on the outer race of the support bearing. The sampling frequency and data length were 13,529 Hz and 100,000 points, respectively. Fig. 20 illustrates the support bearing outer race with small defect. The geometric dimensions and fault defect frequencies of support bearing are listed in Table 2 and Table 3, respectively.

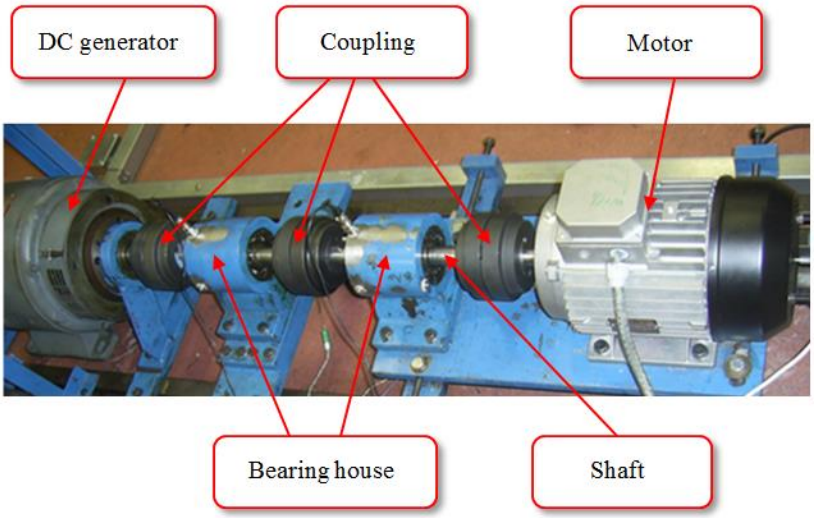

Fig. 19. The bearing test platform.

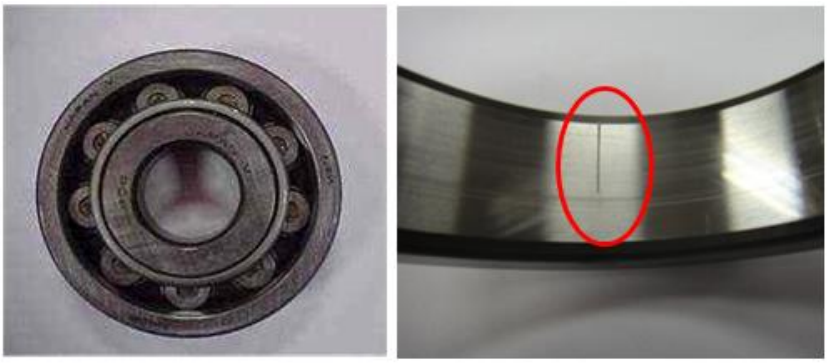

Fig. 20. The support bearing outer race with small defect.

Table 2. Geometric dimensions of the support bearing.

Parameter	Value
Ball diameter (mm)	14
Pitch diameter (mm)	59

Ball numbers	9
Contact angle	0°

Table 3. Fault defect frequencies of the support bearing.

Frequency column	Value (Hz)
Inner race f_i	135.1
Outer race f_o	83.3
Rolling element f_b	48.3
Fundamental cage f_c	9.3

6.1.2. Results and analysis

The waveform, spectrum and envelope spectrum of the vibration signal of the support bearing with the outer race fault are depicted in Fig. 21. From the frequency spectrum, the fault defect frequency f_o and its harmonics cannot be recognized. As depicted in Fig. 21(c), the fault defect frequency f_o is recognized, but its higher order harmonics (i.e. $2f_o$ and $3f_o$) are mixed by background noise and interference harmonics.

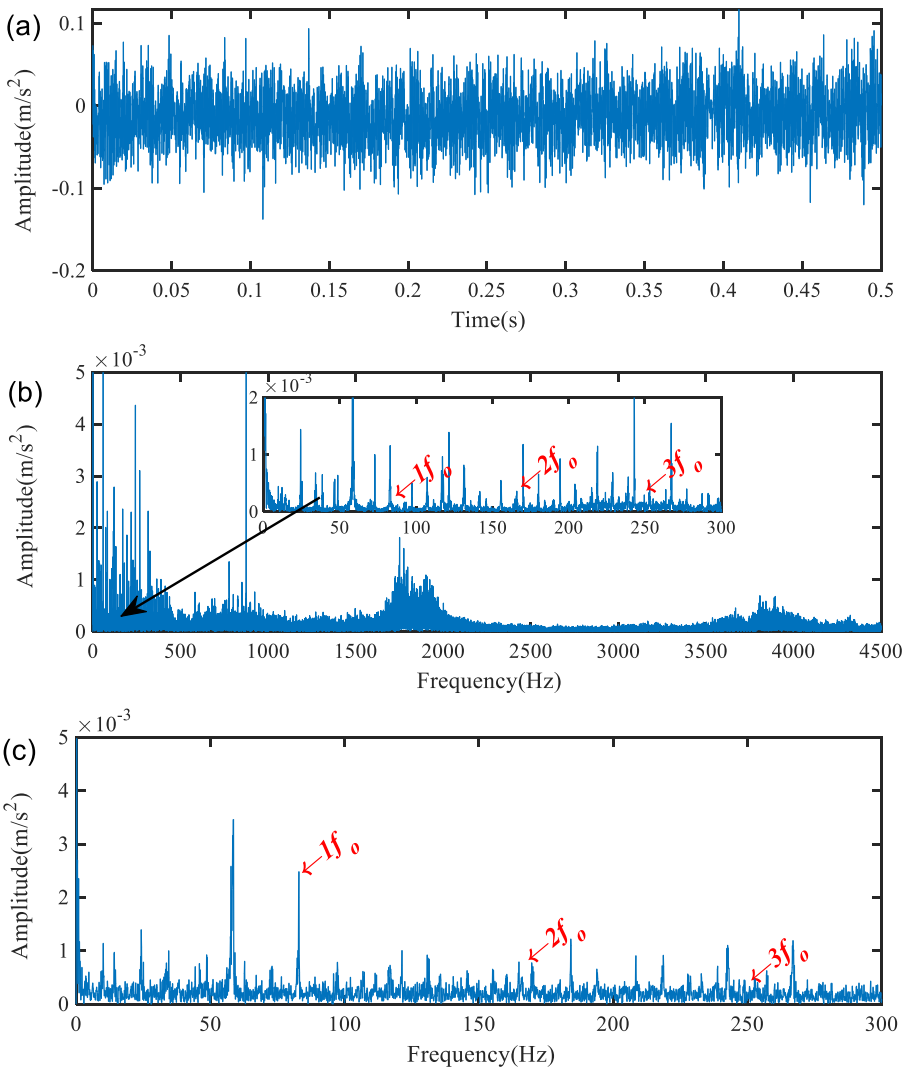

Fig. 21. Vibration signal of the support bearing: (a) waveform (b) spectrum (c) envelope spectrum with central frequency of 1800 Hz and a bandwidth of 400 Hz.

To extract the fault defect frequency f_o and its harmonics, the AMIDIF is exploited to analyze the

support bearing fault signal. To begin with, the faulty bearing signal is decomposed into a certain number of MIDIFs through the AMIDIF. The correlation coefficient u_ε between the MIDIFs and faulty bearing signal, and correlation coefficient φ_ε between the MIDIFs and normal bearing signal are calculated. Afterward, the fault-related coefficients are calculated by the difference between u_ε and φ_ε to remove common information to highlight the useful components of the faulty bearing. At last, the weighted coefficients of the AMIDIF are calculated by normalizing the fault-related coefficients of different scales. The weighted coefficients with different scales of SE are depicted in Fig. 22. The AMIDIF filtered signal is obtained by multiplying the weighted coefficients and MIDIFs under different scales and envelope spectrum are presented in Fig. 23. As displayed in the envelope spectrum, the three main spectrum lines of the support bearing outer race fault are recognized.

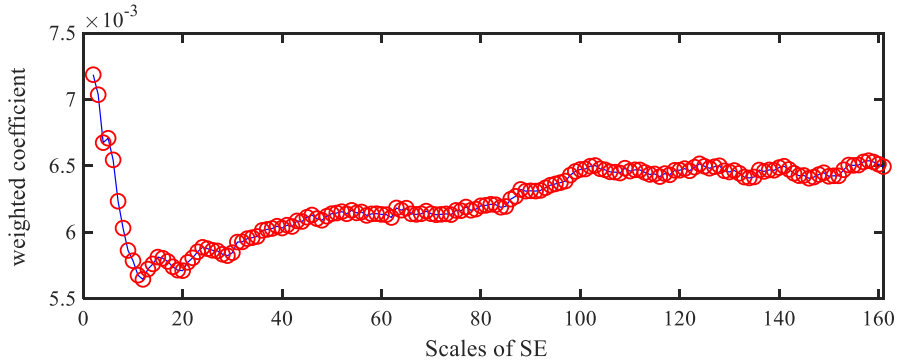

Fig. 22. The weighted coefficient with different scales of SE based on correlation coefficient.

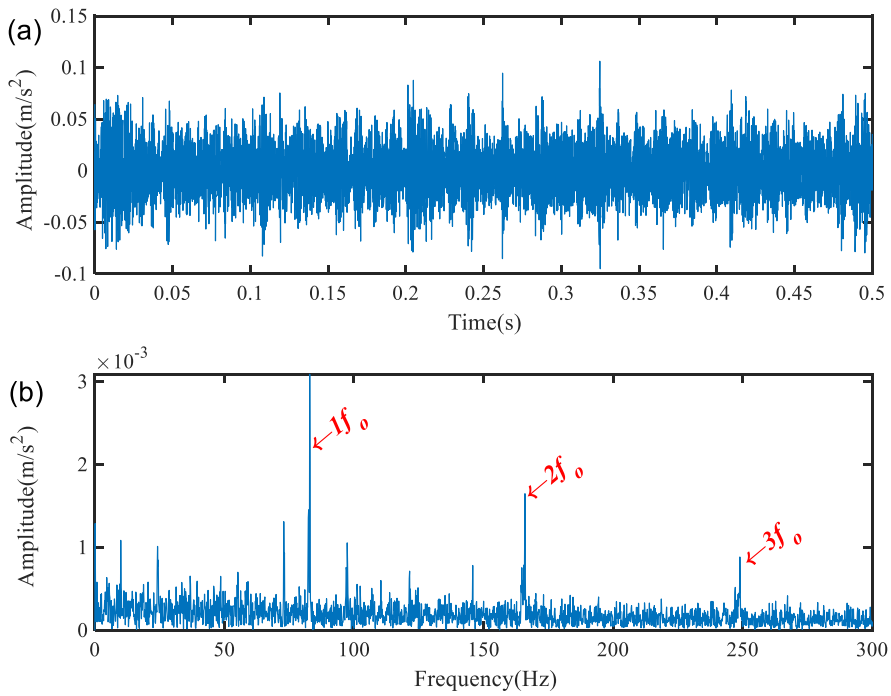

Fig. 23. Processing results of the support bearing by the AMIDIF: (a) waveform (b) envelope spectrum.

For comparison, the multi-scale ACDIF and MGPO methods are utilized to analyze the waveform of Fig. 21(a). The processing results are depicted in Fig. 24 and Fig. 25. As displayed in Fig. 24(b) and Fig. 25(b), only the fault defect frequency f_o can be recognized, but the higher order harmonics (i.e. $2f_o$ and $3f_o$) cannot be identified. Moreover, there are random noise and irrelevant interferences in the low frequencies band. In addition, the same support bearing fault signal is processed by the SK and MOMEDA algorithms, and the obtained results are illustrated in Fig. 26 and Fig. 27. As discovered

in Fig. 26(a), the bandwidth and central frequency of the band pass filter are 422.8 Hz and 1479.7 Hz, respectively. Fig. 26(b) and (c) illustrate envelope and corresponding squared envelope spectrum of the SK. As depicted in Fig. 26(c), the fault defect frequencies (i.e. $f_o, 2f_o$ and $3f_o$) are identified, but the background noise and some interference frequency components are much larger than the processing result presented as Fig. 23(b). The corresponding processing results obtained using the MOMEDA algorithm with the same parameters as the simulation signals are illustrated in Fig. 27. As depicted in Fig. 27(b), the fault defect frequency f_o can be recognized, but the higher order spectrum lines (i.e. $2f_o$ and $3f_o$) of the faulty bearing cannot be identified. To further evaluate the performance of the five algorithms (AMIDIF, ACDIF, MGPO, SK and MOMEDA), the SNR and CPU running time are applied. The contrast results of the five algorithms are illustrated in Table 4. It can be found that the SNR of AMIDIF is higher than the multi-scale difference morphology filters (ACDIF and MGPO), SK and MOMEDA. Although the calculation efficiencies of the SK and MOMEDA are higher than that of the AMIDIF, they cannot accurately extract the main spectrum lines of the faulty bearing. Therefore, the comparison results indicate that the AMIDIF outperforms the other four methods for the support bearing fault detection.

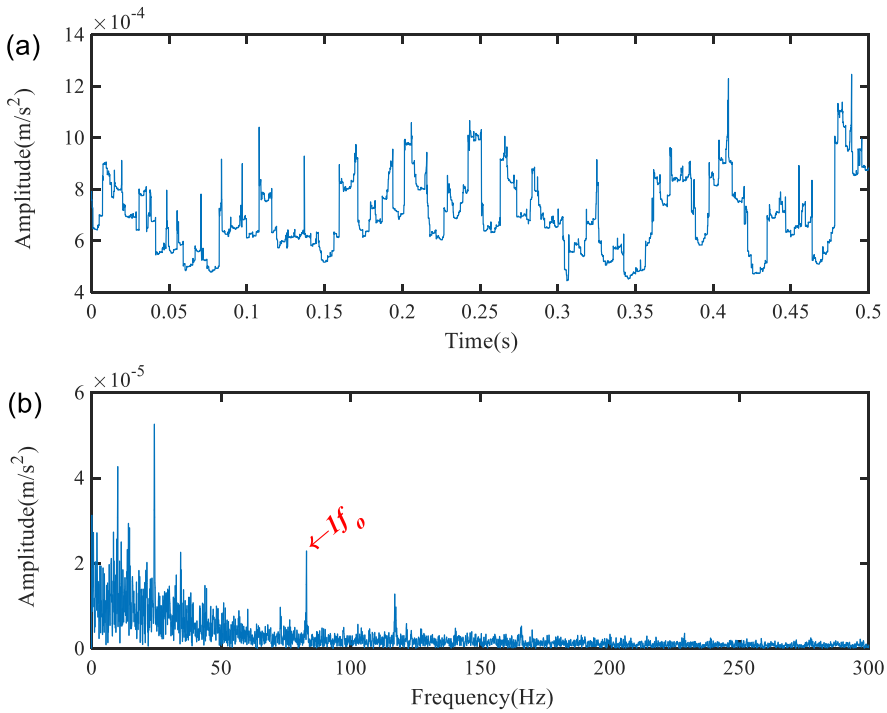

Fig. 24. Processing results of the support bearing by the MGPO: (a) waveform (b) envelope spectrum.

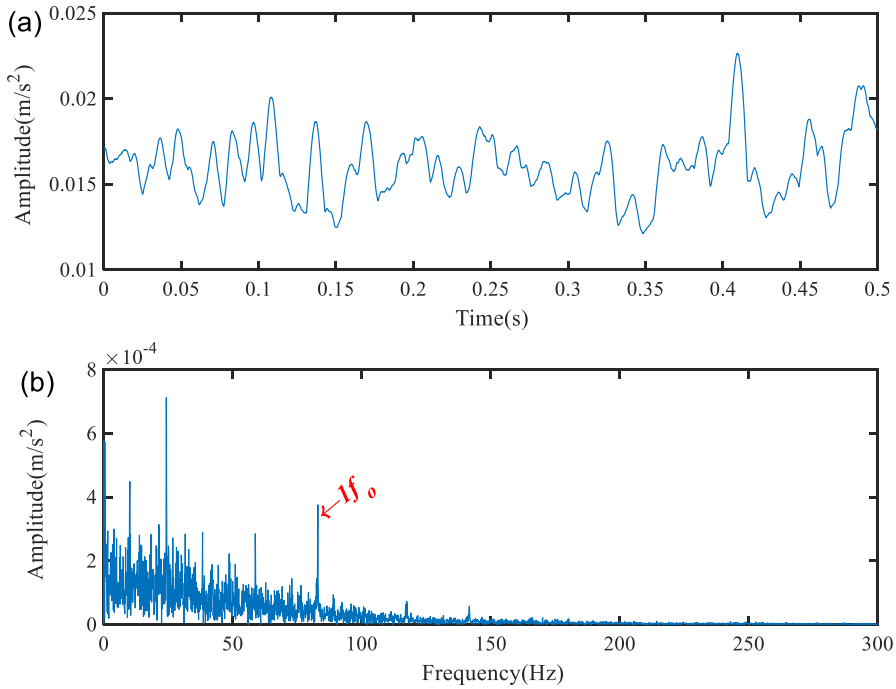

Fig. 25. Processing results of the support bearing by the ACDIF: (a) waveform (b) envelope spectrum.

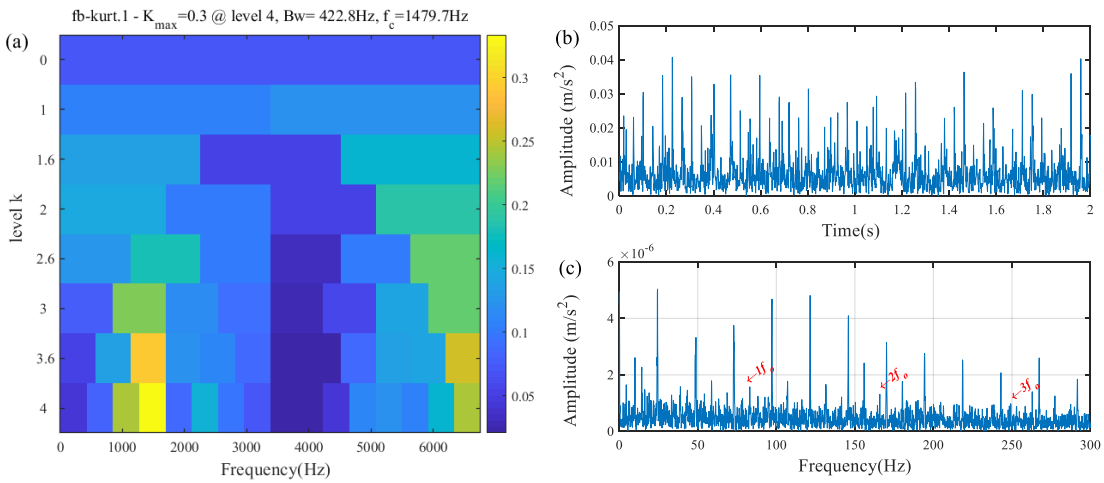

Fig. 26. Processing results of the support bearing by the SK: (a) kurtogram (b) envelope (c) squared envelope spectrum.

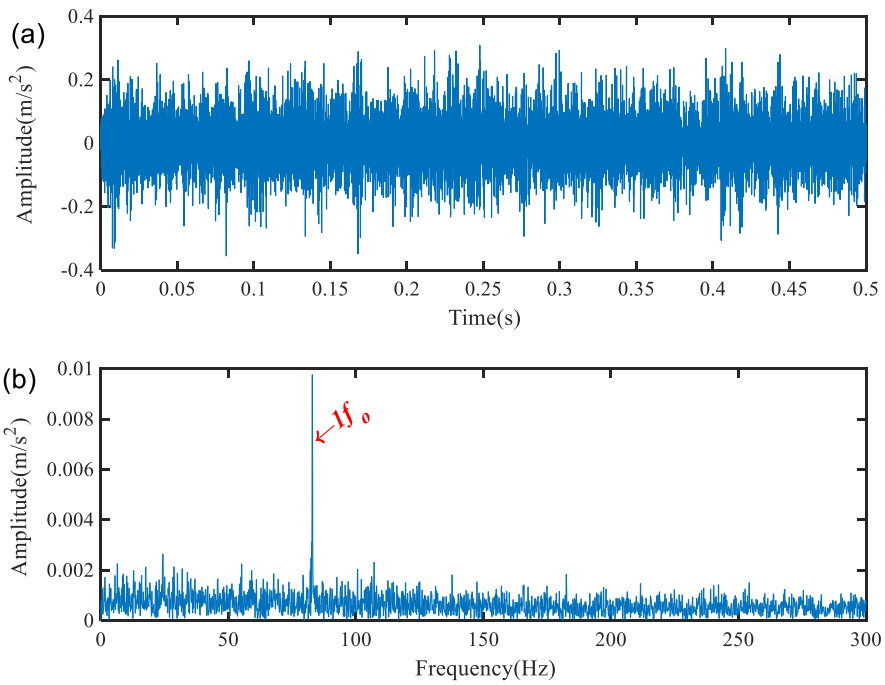

Fig. 27. Processing results of the support bearing by the MOMEDA: (a) waveform (b) envelope spectrum.

Table 4. The contrast results between the AMIDIF and other four algorithms.

Algorithms	SNR	CPU running time (s)
AMIDIF	1.177	125.347
ACDIF	-11.549	363.358
MGPO	-0.381	261.458
SK	-0.004	9.423
MOMEDA	-8.428	4.352

For further comparison study, the support bearing vibration signals are collected under variable conditions from 0%, 50% and 100% loads to monitor the influence of working conditions on fault diagnosis. In addition, the fault defect index is applied to assess the performance of AMIDIF in obtaining fault features under variable conditions in this study. Fig. 28 illustrates the diagnosis results of support bearing under variable conditions by using five algorithms. It can be observed from Fig. 28, the AMIDIF has stronger fault feature extraction capabilities compared with the other four algorithms under any loads.

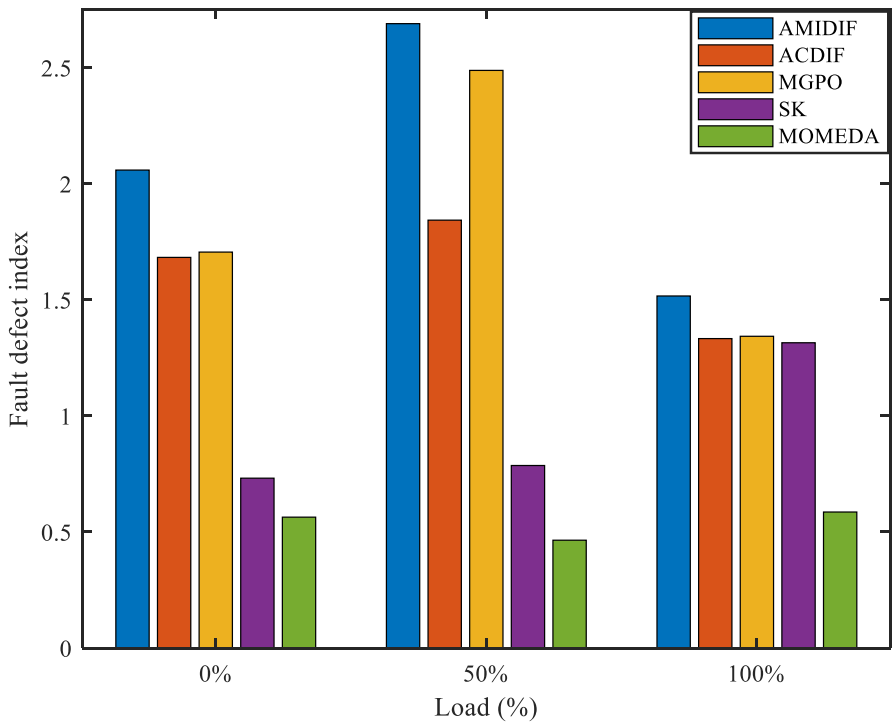

Fig. 28. Fault defect index of five algorithms under variable conditions.

6.2. Case 2: planetary gearbox fault diagnosis

6.2.1. Test setup and data collection

The planetary gearbox test rig is displayed in Fig. 29. It primarily involves an induction motor, a helical gearbox, a planetary gearbox, two flexible type couplings, and a DC generator. In addition, the required speed and load are controlled through a variable speed controller, which sends the require values to the motor and the DC generator. The vibration signal of the planetary gearbox was measured via an accelerometer fixed on top of the planetary gearbox. The sampling frequency and data length were 100,000 Hz and 3000,000 points, respectively. Fig. 30 illustrates the sun gear chipping. The geometric dimensions and fault defect frequencies of planetary gearbox are listed in Table 5 and Table 6, respectively.

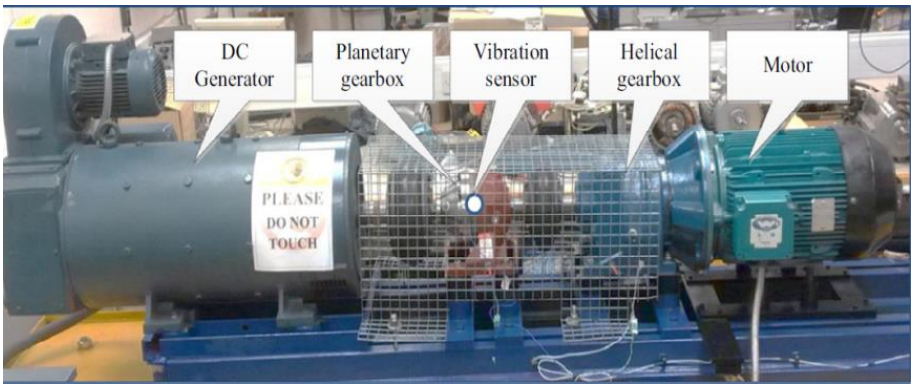

Fig. 29. The planetary gearbox test rig.

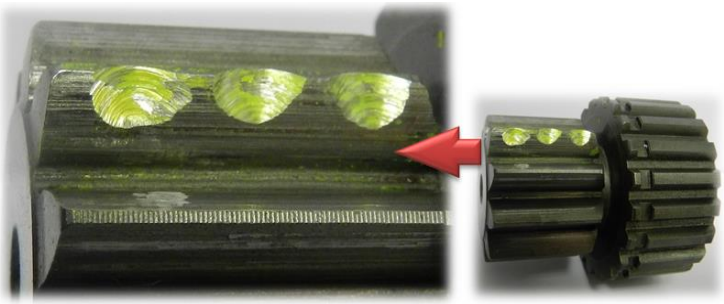

Fig. 30. The sun gear chipping.

Table 5. Geometric dimensions of the planetary gearbox.

Parameter	Number of teeth
Sun gear	10
Planet gear (number)	26(3)
Ring gear	62
Carrier	-

Table 6. Fault defect frequencies of the planetary gearbox.

		Rotational frequency (Hz)	Meshing frequency (Hz)	Fault characteristic frequency (Hz)
Planetary gearbox	Sun gear	9.36	80.61	24.18
	Planet gear	3.60		9.80
	Ring gear	-		3.90
	Carrier	1.30	-	-

6.2.2. Results and analysis

The waveform, spectrum and envelope spectrum of the vibration signal of the planetary gearbox with sun gear chipping are displayed in Fig. 31. From the frequency spectrum, the fault defect frequencies of the sun gear chipping cannot be recognized. As displayed in Fig. 31(c), the sun gear fault defect frequencies (f_{sf} and $2f_{sf}$) and their combinations $f_{sf} \pm f_{rs}$ and $2f_{sf} - f_{rs}$ can be recognized, but the sun gear rotational frequency f_{rs} and their combinations $2f_{sf} + f_{rs}$ cannot be identified.

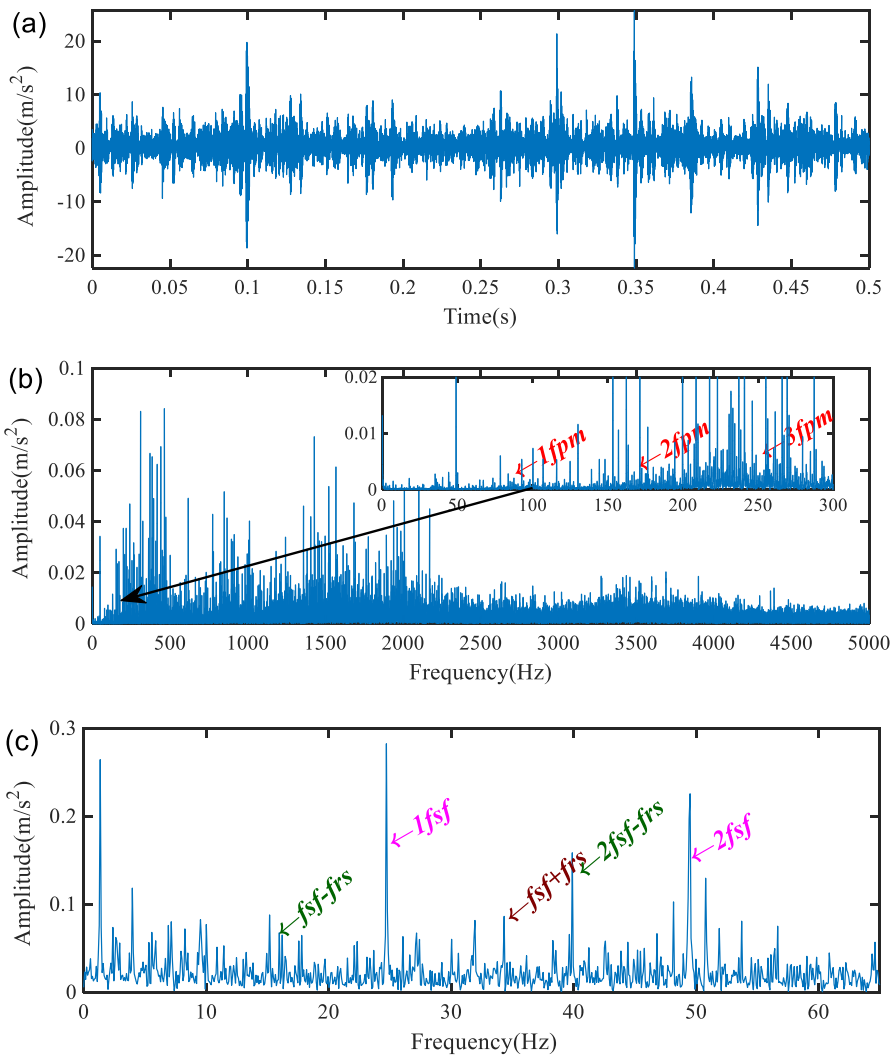

Fig. 31. Vibration signal of the sun gear chipping: (a) waveform (b) spectrum (c) envelope spectrum with central frequency of 80 Hz and a bandwidth of 40Hz.

To extract the fault defect frequency and its harmonics, the AMIDIF is utilized to analyze the sun gear chipping signal. First of all, the sun gear chipping vibration signals are decomposed into a series of MIDIFs using the AMIDIF. The correlation coefficient u_ε between the sun gear chipping signal and its MIDIFs, and correlation coefficient φ_ε between the MIDIFs and normal sun gear signal are calculated. Subsequently, the fault-related coefficients are calculated by the difference between u_ε and φ_ε to obtain the useful components of the sun gear chipping. Finally, the weighted coefficients of AMIDIF are calculated by normalizing the fault-related coefficients of different scales. Due to the fault defect frequency of the sun gear chipping is very small and the sampling frequency is too large, the SE scale of the AMIDIF will be too large. Therefore, to simplify the calculation, the SE scale of the AMIDIF is limited to 1-200. The weighted coefficients with different scales of SE are depicted in Fig 32. The AMIDIF filtered signal is obtained by multiplying the weighted coefficients and MIDIFs under different scales and envelope spectrum are drawn in Fig. 33. As depicted in the envelope spectrum, the sun gear rotational frequency f_{rs}, sun gear defect frequency f_{sf} and their combinations $f_{sf}\pm f_{rs}$ can be correctly recognized.

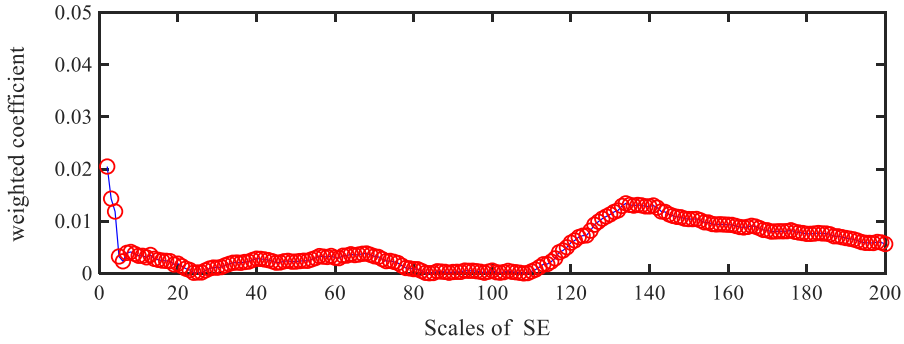

Fig. 32. The weighted coefficient with different scales of SE based on correlation coefficient.

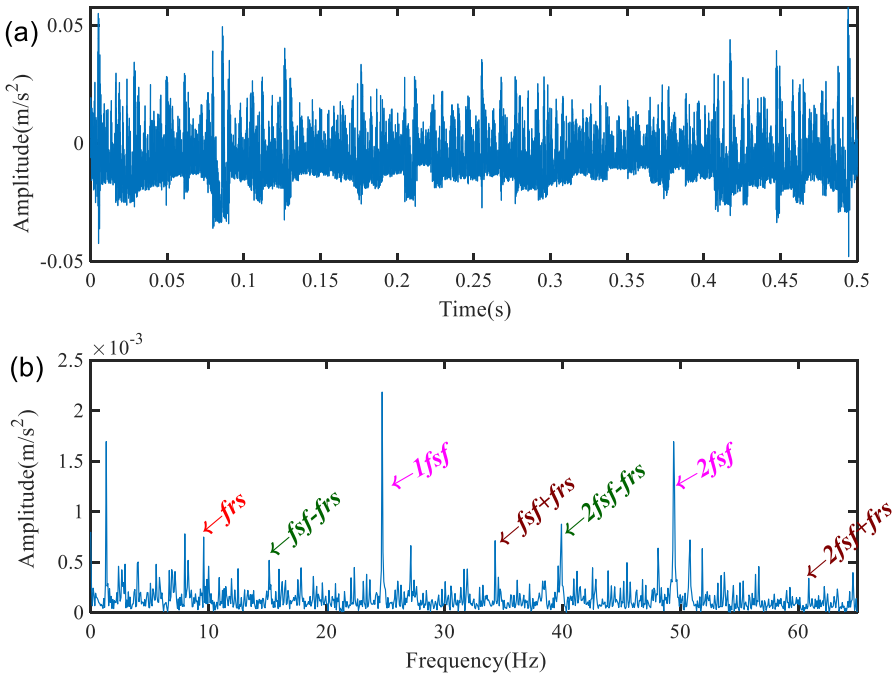

Fig. 33. Processing results of the sun gear chipping by the AMIDIF: (a) waveform (b) envelope spectrum.

As comparisons, the multi-scale difference morphology filters (ACDIF and MGPO) are used to analyze the waveform of Fig. 31(a). The MGPO filtered results with different scales of SE based on FEF and envelope spectrum are depicted in Fig. 34. Only the sun gear fault defect frequencies f_{sf} and its harmonics and their combinations $f_{sf}+f_{rs}$ and $2f_{sf}-f_{rs}$ can be recognized. The multi-scale ACDIF filtered results with different scales of SE based on TEK and corresponding envelope spectrum are drawn in Fig. 35. It can be found that the sun gear rotational frequency f_{rs}, sun gear defect frequency f_{sf} and its harmonics and their combinations $f_{sf}-f_{rs}$ can be observed, but the their combinations $f_{sf}+f_{rs}$ and $2f_{sf}\pm f_{rs}$ cannot be identified. Similarly, the sun gear chipping signal is handled by the SK and MOMEDA algorithms. As discovered in Fig. 36(a), the bandwidth and central frequency of the band pass filter are 250 Hz and 1625 Hz, respectively. The envelope and squared envelope spectrum of the filtered signal using SK are illustrated in Fig. 36(b) and (c). As depicted in Fig. 36(c), the sun gear rotational frequency f_{rs}, sun gear fault defect frequencies f_{sf} and its harmonics and their combinations $f_{sf}+f_{rs}$ and $2f_{sf}-f_{rs}$ can be found, and there are some interference frequency components. The processing

results obtained using the MOMEDA algorithms are depicted in Fig. 37. As drawn in Fig. 37(b), the sun gear rotational frequency f_{rs}, sun gear defect frequency f_{sf} and its harmonics and their combinations $f_{sf}-f_{rs}$ and $2f_{sf}-f_{rs}$ can be observed, but the their combinations $2f_{sf}+f_{rs}$ and $f_{sf}+f_{rs}$ cannot be identified. The SNR and CPU running time of the five methods (AMIDIF, ACDIF, MGPO, SK and MOMEDA) are shown in Table 7. It can be found that the AMIDIF is less efficient than the SK and MOMEDA algorithms, but the fault feature extraction capability of the AMIDIF is higher than the other four algorithms. Hence, the comparison results illustrate that the AMIDIF is better than the other four algorithms in the sun gear chipping fault diagnosis.

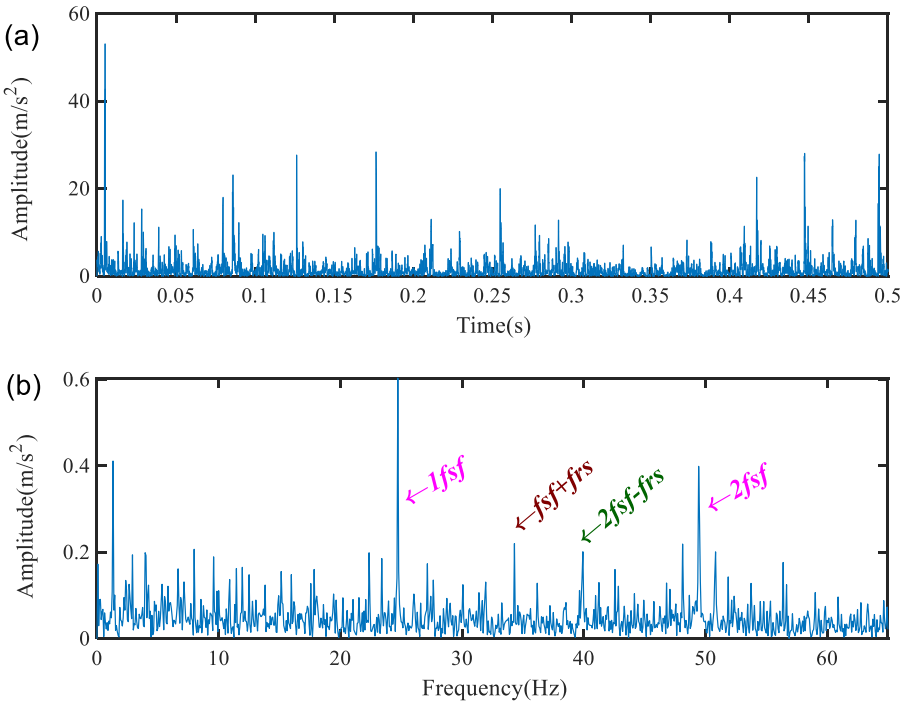

Fig. 34. Processing results of the sun gear chipping by the MGPO: (a) waveform (b) envelope spectrum.

Table 7. The contrast results between the AMIDIF and other four algorithms.

Algorithms	SNR	CPU running time (s)
AMIDIF	0.010	390.377
ACDIF	-6.392	1342.231
MGPO	-18.239	1228.227
SK	0.003	14.009
MOMEDA	-6.221	8.845

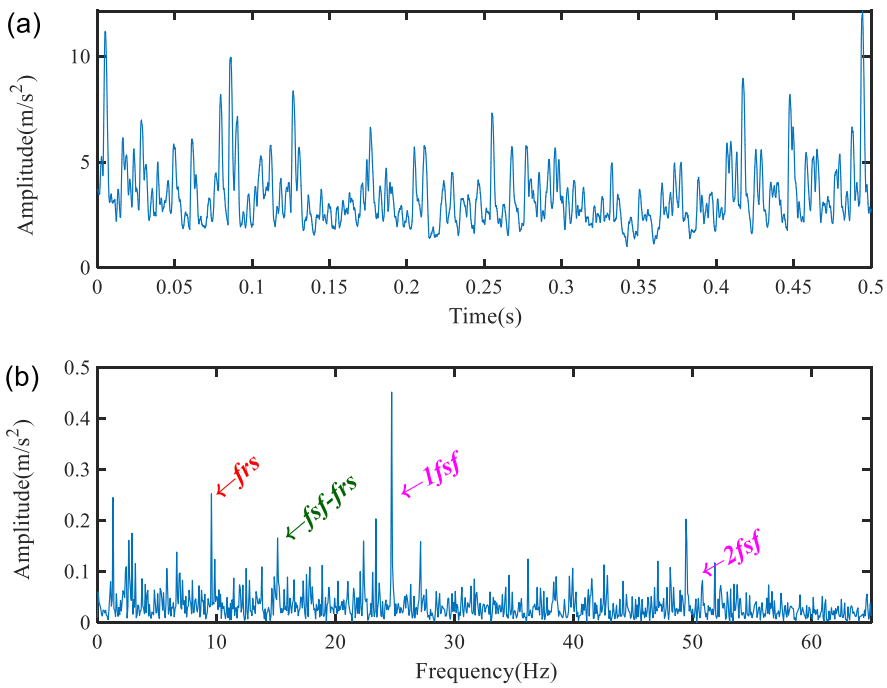

Fig. 35. Processing results of the sun gear chipping by the ACDIF: (a) waveform (b) envelope spectrum.

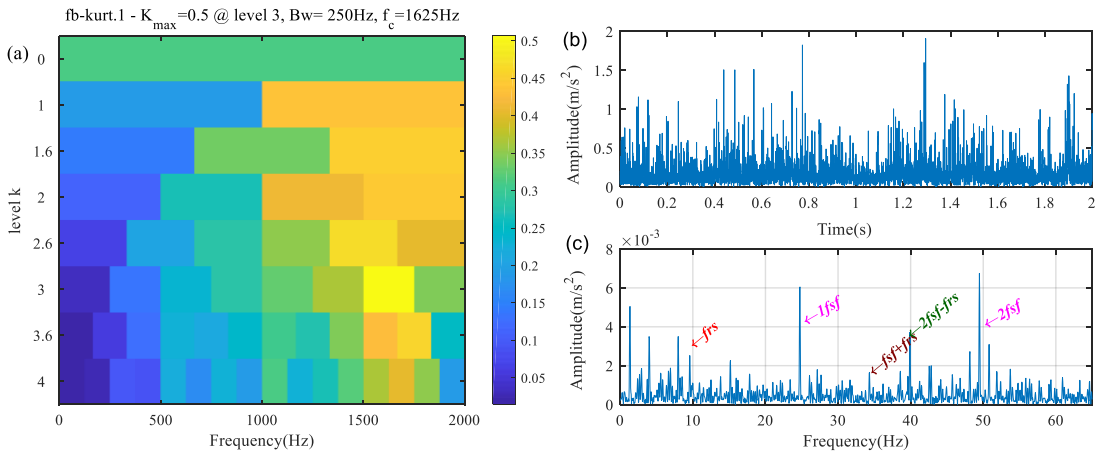

Fig. 36. Processing results of the sun gear chipping by the SK: (a) kurtogram (b) envelope (c) squared envelope spectrum.

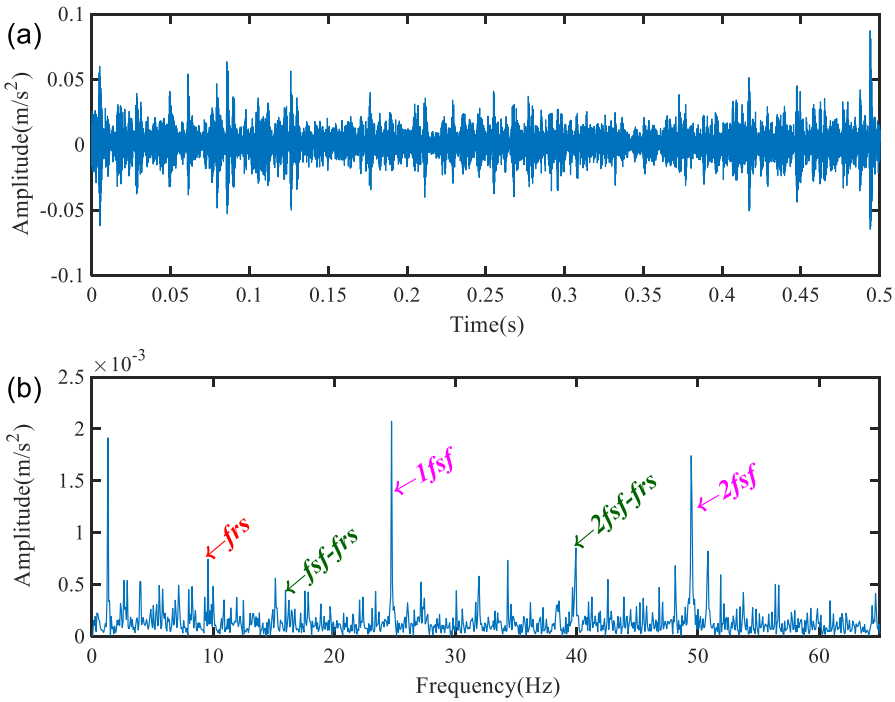

Fig. 37. Processing results of the sun gear chipping by the MOMEDA: (a) waveform (b) envelope spectrum.

In order to further comparison study, the sun gear chipping vibration signals are collected under variable conditions from 0%, 25%, 50%, 75% and 90% loads. The detection results of sun gear chipping under variable conditions with five algorithms are presented in Fig. 38. It can be observed that the AMIDIF has stronger fault feature extraction capabilities compared with the other four algorithms under variable conditions. It is essential to note that the fault defect index value of the SK is higher than that of the AMIDIF under 75% load. The reason for this phenomenon may be that the frequency band selected by the SK using the kurtosis value is more accurate under 75% load. Overall, the AMIDIF can more accurately realize the planetary gearbox fault diagnosis contrast with the four methods (ACDIF, MGPO, SK and MOMEDA).

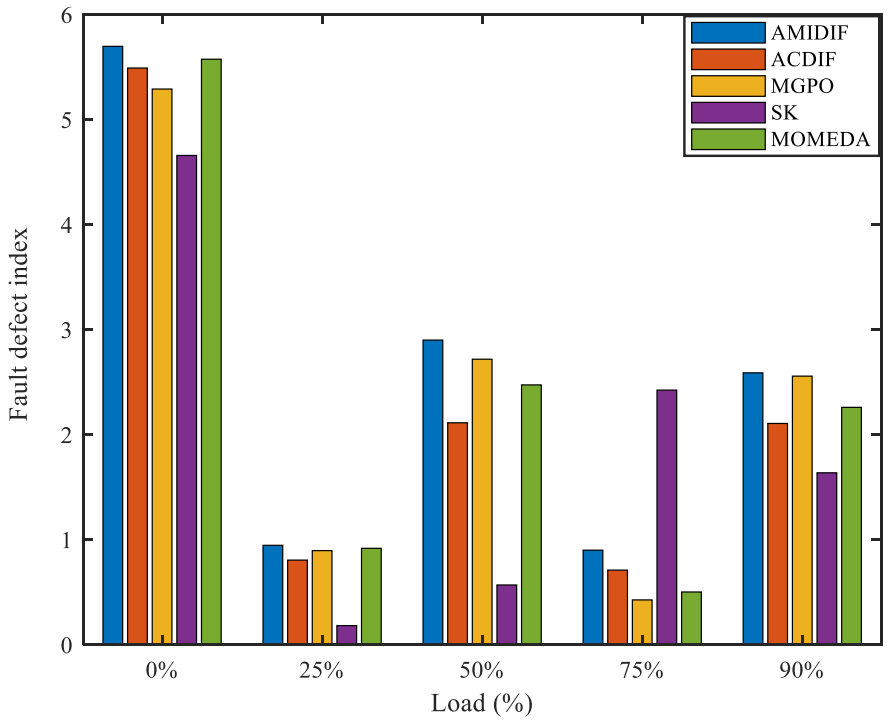

Fig. 38. Fault defect index of five algorithms under variable conditions.

7. Conclusion

In this paper, an adaptive multi-scale morphological filter named AMIDIF is proposed, which can effectively remove the interference of random noise and harmonic frequencies to enhance transient impulses. To solve the issue of manual selection of the weighted coefficients in AMIDIF, a weighted reconstruction algorithm based on correlation coefficient is presented in which the weighted coefficients are counted and distributed to the corresponding MIDIF filtered signals to highlight the useful MIDIFs and reduce the interference from other MIDIFs. The feasibility of the AMIDIF is demonstrated through a numerical simulation and experimental cases of bearing with outer race fault and planetary gearbox with sun gear chipping. The results illustrate that the AMIDIF has great benefits for transient impulses enhancement. In addition, the AMIDIF is superior to the multi-scale difference morphology filters (i.e. ACDIF and MGPO), SK and MOMEDA in fault feature extraction. However, the AMIDIF still has some shortcomings that need to be researched and improved. On the one hand, although the AMIDIF is superior to the existing multi-scale morphological filters (i.e. ACDIF and MGPO) in accuracy improvement, it still needs spend a lot of running time in data analysis with low computational efficiency, which cannot be applied in online condition monitoring. On the other hand, the effectiveness of the AMIDIF in extracting fault features will be reduced in the case lower SNR. Thus, the above mentioned issues need to be paid more attention in the future research.

Acknowledgement

The work is supported by the National Natural Science Foundation of China under Grant Nos. 51875166, 51705127 and U1813222.

References

[1] Wang T, Han Q, Chu F, Feng Z. Vibration based condition monitoring and fault diagnosis of wind

turbine planetary gearbox: a review. Mech Syst Signal Process 2019; 126: 662-85.
[2] Yang B, Yang Z, Sun R, Zhai Z, Chen X. Fast nonlinear chirplet dictionary-based sparse decomposition for rotating machinery fault diagnosis under nonstationary conditions. IEEE Trans Instrum Meas 2019; 68 (12): 4736-45.
[3] Lei Y, Liu Z, Lin J, Lu F. Phenomenological models of vibration signals for condition monitoring and fault diagnosis of epicyclic gearboxes. J Sound Vib 2016; 369: 266-81.
[4] Cui L, Wang X, Wang H, Ma J. Research on remaining useful life prediction of rolling element bearings based on time-varying kalman filter. IEEE Trans Instrum Meas 2020; 69(6): 2858-67.
[5] Wang T, Chu F. Bearing fault diagnosis under time-varying rotational speed via the fault characteristic order (FCO) index based demodulation and the stepwise resampling in the fault phase angle (FPA) domain. ISA Trans 2019; 94: 391-400.
[6] Guo J, Zhen D, Li H, Shi Z, Gu F, Ball AD. Fault detection for planetary gearbox based on an enhanced average filter and modulation signal bispectrum analysis. ISA Trans 2020; 101: 408-20.
[7] Saidi L, Ali JB, Fnaiech F. Bi-spectrum based-EMD applied to the non-stationary vibration signals for bearing faults diagnosis. ISA Trans 2014; 53 (5): 1650-60.
[8] Yaslan Y, Bican B. Empirical mode decomposition based denoising method with support vector regression for time series prediction: A case study for electricity load forecasting. Measurement 2017; 103: 52-61.
[9] Li Y, Liang X, Xu M, Huang W. Early fault feature extraction of rolling bearing based on ICD and tunable Q-factor wavelet transform. Mech Syst Signal Process 2017; 86: 204-23.
[10] Pachori RB, Nishad A. Cross-terms reduction in the Wigner-Ville distribution using tunable-Q wavelet transform. Signal Process 2016; 120: 288-304.
[11] Zhang X, Wang J, Liu Z, Wang J. Weak feature enhancement in machinery fault diagnosis using empirical wavelet transform and an improved adaptive bistable stochastic resonance. ISA Trans 2019; 84: 283-95.
[12] Li J, Wang H, Zhang J, Yao X, Zhang Y. Impact fault detection of gearbox based on variational mode decomposition and coupled underdamped stochastic resonance. ISA Trans 2019; 95: 320-29.
[13] Yan X, Jia M. Application of CSA-VMD and optimal scale morphological slice bispectrum in enhancing outer race fault detection of rolling element bearings. Mech Syst Signal Process 2019; 122: 56-86.
[14] Miao Y, Zhao M, Yi Y, Lin J. Application of sparsity-oriented VMD for gearbox fault diagnosis based on built-in encoder information. ISA Trans 2020; 99: 496-504.
[15] Hu AJ, Sun JJ, Xiang L. Analysis of morphological filter's frequency response characteristics in vibration signal processing. Chin J Mech Eng 2012; 48 (1): 98-103.
[16] Nikolaou NG, Antoniadis IA. Application of morphological operators as envelope extractors for impulsive-type period signals. Mech Syst Signal Process 2003; 17 (6): 1147-62.
[17] Wang J, Xu G, Zhang Q, Liang, L. Application of improved morphological filter to the extraction of impulsive attenuation signals. Mech Syst Signal Process 2009; 23 (1): 236-45.
[18] Hu Z, Wang C, Zhu J, Liu X, Kong F. Bearing fault diagnosis based on improved morphological filter. Measurement 2016; 80: 163-78.
[19] Zhang L, Xu J, Yang J, Yang D, Wang D. Multiscale morphology analysis and its application to fault diagnosis. Mech Syst Signal Process 2008; 22: 597-610.
[20] Osman S, Wang W. A morphological Hilbert-Huang transform technique for bearing fault detection. IEEE. Trans. Instrum. Meas. 2016; 65(11): 2646-56.

[21] Raj AS, Murali N. Early classification of bearing faults using morphological operators and fuzzy inference. IEEE Trans Industr Electron 2013; 60 (2): 567-74.
[22] Li Y, Liang X, Zuo MJ. Diagonal slice spectrum assisted optimal scale morphological filter for rolling element bearing fault diagnosis. Mech Syst Signal Process 2017; 85: 146-61.
[23] Dong Y, Liao M, Zhang X. Wang F. Faults diagnosis of rolling element bearings based on modified morphological method. Mech Syst Signal Process 2011; 25 (3): 1276-86.
[24] Hu A, Xiang L. Selection principle of mathematical morphological operators in vibration signal processing. J Vib Control 2014; 1-12.
[25] Meyer F. Iterative image transforms for an automatic screening of cervical smears. J Histochem Cytochem 1979; 27 (1): 128-35.
[26] Li B, Zhang PL, Wang ZJ, Mi SS, Zhang YT. Gear fault detection using multi-scale morphological filters. Measurement 2011; 44 (10): 2078-89.
[27] Li B, Zhang PL, Wang ZJ, Mi SS, Liu DS. A weighted multi-scale morphological gradient filter for rolling element bearing fault detection. ISA Trans 2011; 50 (4): 599-608.
[28] Li Y, Zuo MJ, Lin J, Liu J. Fault detection method for railway wheel flat using an adaptive multiscale morphological filter. Mech Syst Signal Process 2017; 84: 642-58.
[29] Deng F, Yang S, Tang G, Hao R, Zhang M. Self adaptive multi-scale morphology AVG-Hat filter and its application to fault feature extraction for wheel bearing. Meas Sci Technol 2017; 28 (4): 045011.
[30] Yan X, Jia M, Zhang W, Zhu L. Fault diagnosis of rolling element bearing using a new optimal scale morphology analysis method. ISA Trans 2018; 73: 165-80.
[31] Li C, Liang M. Continuous-scale mathematical morphology-based optimal scale band demodulation of impulsive feature for bearing defect diagnosis. J Sound Vib 2012; 331 (26): 5864-79.
[32] Serra J. Image analysis and mathematical morphology. Academic Press, New York, USA, 1982.
[33] Li Y, Zuo MJ, Chen Z, Lin J. Railway bearing and cardan shaft fault diagnosis via an improved morphological filter. Struct Healt Monitor 2019; 19(5): 1471-86.
[34] Jiang W, Zheng Z, Zhu Y, Yi Ye. Demodulation for hydraulic pump fault signals based on local mean decomposition and improved adaptive multiscale morphology analysis. Mech Syst Signal Process 2015; 58-59: 179-205.
[35] Chen Q, Chen Z, Sun W. A new structuring element for multi-scale morphology analysis and its application in rolling element bearing fault diagnosis. J Vib Control 2015; 21 (4): 765-89.
[36] Lei Y, Zuo MJ, Hoseini M. The use of ensemble empirical mode decomposition to improve bispectral analysis for fault detection in rotating machinery. Proceedings of the Institution of Mechanical Engineers, Part C: Journal of Mechanical Engineering Science 2010; 224 (8): 1759-69.
[37] Gong T, Yuan X, Lei X, Yuan Y, Zhang B. Fault detection for rolling element bearing based on repeated single-scale morphology and simplified sensitive factor algorithm. Measurement 2018; 127 348-55.
[38] Cheng Y, Zhou N, Zhang W, Wang Z. Application of an improved minimum entropy deconvolution method for railway rolling element bearing fault diagnosis. J Sound Vib 2018; 425: 53-69.
[39] Miao Y, Zhao M, Lin J, Lei Y. Application of an improved maximum correlated kurtosis deconvolution method for fault diagnosis of rolling element bearings. Mech Syst Signal Process 2017; 92: 173-95.
[40] Guo J, Zhang H, Zhen D, Shi Z, Gu F, Ball AD. An enhanced modulation signal bispecturm analysis for bearing fault detection based on non-Gaussian noise suppression. Measurement 2019; 151: 107240.
[41] Cheng Y, Wang Z, Zhang W, Huang G. Particle swarm optimization algorithm to solve the

deconvolution problem for rolling element bearing fault diagnosis. ISA Trans 2019; 90: 244-67.
[42] Lv JX, Yu JB. Average combination difference morphological filters for fault feature extraction of bearing. Mech Syst Signal Process 2018; 100: 827-45.
[43] Li Y, Zuo MJ, Chen Y, Feng K. An enhanced morphology gradient product filter for bearing fault detection. Mech Syst Signal Process 2018; 109: 166-84.
[44] Antoni J, Randall RB. The spectral kurtosis: application to the vibratory surveillance and diagnostics of rotating machines. Mech Syst Signal Process 2006; 20(2): 308-31.
[45] McDonald, GL, Zhao, Q. Multipoint optimal minimum entropy deconvolution and convolution fix: application to vibration fault detection. Mech Syst Signal Process 2017; 82: 461-77.
[46] Wang Z, Du W, Wang J, Zhou J, Han X, Zhang Z, Huang L. Research and application of improved adaptive MOMEDA fault diagnosis method. Measurement 2019; 140: 63-75.
[47] Ma H, Feng Z. Planet bearing fault diagnosis using multipoint optimal minimum entropy deconvolution adjusted. J Sound Vib 2019; 449: 235-73.
[48] Wang B, Zhang X, Sun C, Chen, X. A quantitative intelligent diagnosis method for early weak faults of aviation high-speed bearings. ISA Trans 2019; 93: 370-83.
[49] Cheng Y, Zhou N, Zhang W, Wang Z. Application of an improved minimum entropy deconvolution method for railway rolling element bearing fault diagnosis. J Sound Vib 2018; 425: 53-69.